UC Irvine
UC Irvine Previously Published Works

Title
Hindcasts of potential harmful algal bloom transport pathways on the Pacific Northwest coast

Permalink
https://escholarship.org/uc/item/5x79v8nq

Journal
Journal of Geophysical Research - Oceans, 119(4)

ISSN
2169-9275

Authors
Giddings, SN
MacCready, P
Hickey, BM
et al.

Publication Date
2014-04-01

DOI
10.1002/2013jc009622

Peer reviewed

eScholarship.org Powered by the California Digital Library
University of California

AGU PUBLICATIONS

JGR

Journal of Geophysical Research: Oceans

RESEARCH ARTICLE

10.1002/2013JC009622

Hindcasts of potential harmful algal bloom transport pathways on the Pacific Northwest coast

S. N. Giddings[1,2], P. MacCready[1], B. M. Hickey[1], N. S. Banas[3], K. A. Davis[4], S. A. Siedlecki[3], V. L. Trainer[5], R. M. Kudela[6], N. A. Pelland[1], and T. P. Connolly[1]

[1]School of Oceanography, University of Washington, Seattle, Washington, USA, [2]Now at Scripps Institution of Oceanography, UC San Diego, La Jolla, California, USA, [3]Joint Institute for the Study of the Atmosphere and Ocean, Seattle, Washington, USA, [4]Department of Civil & Environmental Engineering, UC Irvine, Irvine, California, USA, [5]NOAA Northwest Fisheries Science Center, Seattle, Washington, USA, [6]Department of Ocean Sciences, UC Santa Cruz, Santa Cruz, California, USA

Key Points:
- Potential PNW HAB transport is seasonal, consistent with regional currents
- Transport is blocked by the Columbia River plume unless entrainment occurs
- A coupled hydrodynamic-biological model can predict PNW *Pn* HAB transport paths

Correspondence to:
S. N. Giddings,
sarahgid@ucsd.edu

Citation:
Giddings, S. N., P. MacCready, B. M. Hickey, N. S. Banas, K. A. Davis, S. A. Siedlecki, V. L. Trainer, R. M. Kudela, N. A. Pelland, and T. P. Connolly (2014), Hindcasts of potential harmful algal bloom transport pathways on the Pacific Northwest coast, *J. Geophys. Res. Oceans*, *119*, 2439–2461, doi:10.1002/2013JC009622.

Received 19 NOV 2013
Accepted 17 MAR 2014
Accepted article online 20 MAR 2014
Published online 16 APR 2014

Abstract Harmful algal blooms (HABs) pose a significant threat to human and marine organism health, and negatively impact coastal economies around the world. An improved understanding of HAB formation and transport is required to improve forecasting skill. A realistic numerical simulation of the US Pacific Northwest region is used to investigate transport pathways from known HAB formation hot spots, specifically for *Pseudo-nitzschia* (*Pn*), to the coast. We show that transport pathways are seasonal, with transport to the Washington (WA) coast from a northern source (the Juan de Fuca Eddy) during the summer/fall upwelling season and from a southern source (Heceta Bank) during the winter/early spring due to the predominant wind-driven currents. Interannual variability in transport from the northern source is related to the degree of wind intermittency with more transport during years with more frequent relaxation/downwelling events. The Columbia River plume acts to mitigate transport to the coast as the plume front blocks onshore transport. The plume's influence on alongshore transport is variable although critical in aiding transport from the southern source to the WA coast via plume entrainment. Overall transport from our simulations captures most observed *Pn* HAB beach events from 2004 to 2007 (characterized by *Pseudo-nitzschia* cell abundance); however, numerous false positives occur. We show that incorporating phytoplankton biomass results from a coupled biogeochemical model reduces the number of false positives significantly and thus improves our *Pn* HAB predictions.

1. Introduction

Harmful algal blooms (HABs) pose a significant and increasing threat to human and marine organism health, and negatively impact coastal economies around the world [*Anderson et al*., 2012]. Certain species of the genus *Pseudo-nitzschia* (*Pn*) are prominent on the US Pacific Northwest (PNW) coast and capable of producing the toxin domoic acid (DA). Although *Pn* and DA are found worldwide, they have been most detrimental in upwelling systems [*Trainer et al*., 2012], systems that are susceptible to a variety of HAB species due to their overall high nutrients and high productivity [*Trainer et al*., 2010; *Pitcher et al*., 2010]. DA can be transferred through the food web to filter-feeding shellfish, which, when ingested by humans, can lead to amnesiac shellfish poisoning. DA toxicity, resulting in long-lasting effects and deaths, has been reported in humans and several species of seabirds and marine mammals [e.g., *Bejarano et al*., 2008]. Implementation of monitoring programs and warning systems has decreased the impact on human health, yet HABs continue to cause environmental damage and economic losses. Conservative closures of harvesting have resulted in significant revenue loss for shellfish and planktivorous fish industries [*Trainer et al*., 2012; *Dyson and Huppert*, 2010]. Thus, an improved understanding of HAB formation (including *Pn* growth and DA production), bloom progression, and physical transport is required to better predict, understand, and mitigate events.

To date, various factors have been implicated in *Pn* HAB formation and DA production and in fact, toxin production may depend on the geographic region [*Trainer et al*., 2012; *Kudela et al*., 2010]. Multiple studies have shown the importance of nutrient input and physical retention to the creation and maintenance of coastal blooms [e.g., *Schnetzer et al*., 2007; *Trainer et al*., 2000; *Pitcher et al*., 2010], yet bloom timing, strength, and toxicity remain difficult to predict. Some of the newest, most promising methods for HAB management include improved detection/monitoring of cells and modeling; including conceptual,

© 2014. American Geophysical Union. All Rights Reserved.

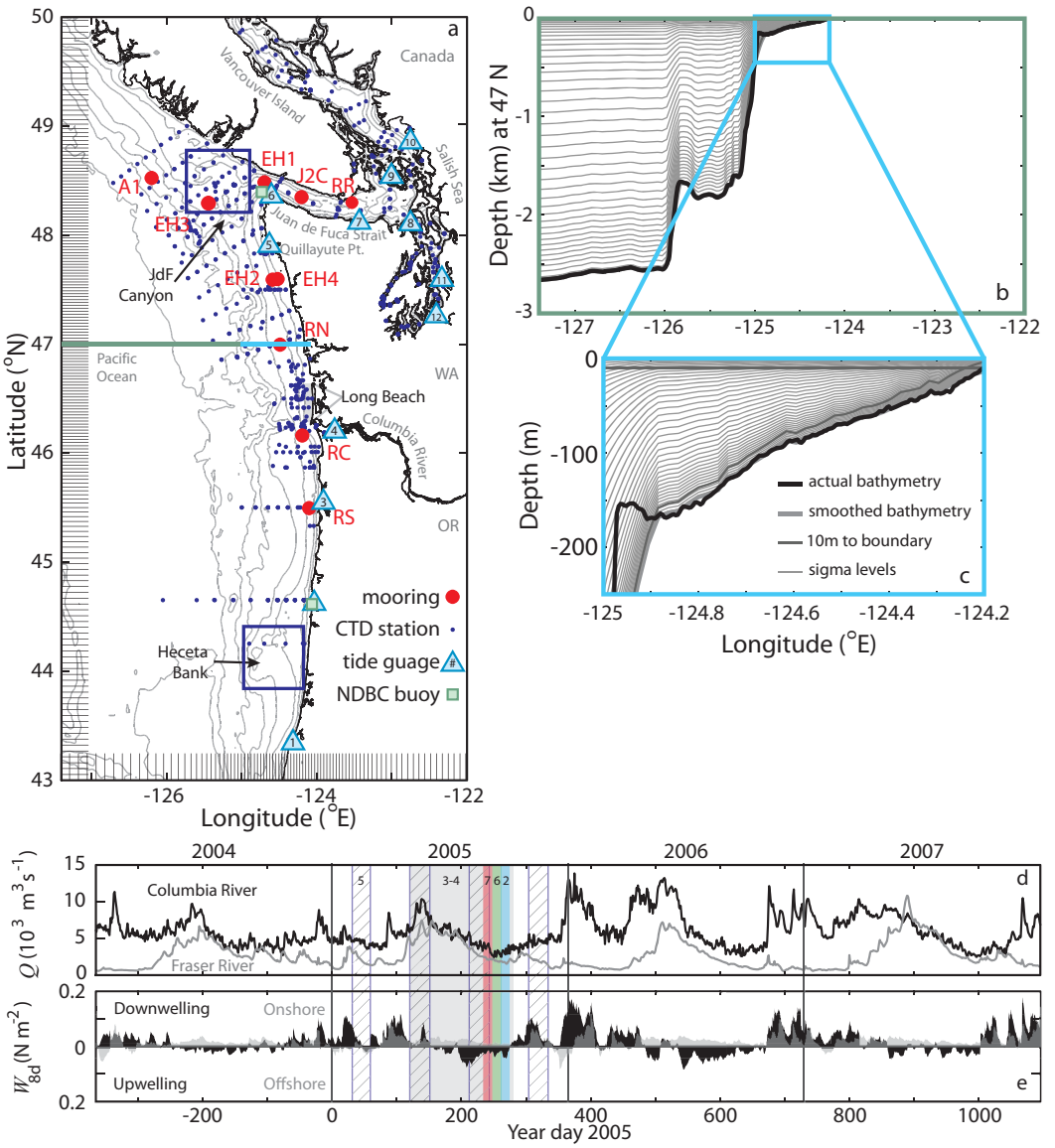

Figure 1. Model domain overlain with moorings (circles), repeat CTD stations (dots), NOAA tide gauges (triangles, numbers correspond to Table 1), and NDBC buoys (squares). Note that the NDBC buoys are colocated with tide gauges 2 and 6. Tick marks on the axes indicate every other grid point in the domain. Bathymetry contours are at 30, 50, 100, 180, 500, 1000, 2000, 3000, and 4000 m depth. Boxes indicate particle release locations and the Long Beach landing location is labeled stretching from just north of the CR mouth to the southern entrance of Willapa Bay. (b) Cross sections at 47°N showing the vertical grid over the entire domain and (c) zoomed in over the shelf. The shelf section (Figure 1c) includes the raw bathymetry (thick black), the smoothed bathymetry (thick gray), the vertical grid spacing on sigma levels (light gray), and a line delineating 10 m from the boundary as an approximation to the upper and lower boundary layers (thin gray). (d) River flow from the two largest rivers and (e) 8 day weighted winds over the full 4 year simulation period computed as described in section 4.1. Winds are rotated into alongshore (black) and cross-shore (gray) principal components where >0 is downwelling favorable and onshore winds, respectively. Vertical bands in Figures 1d and 1e indicate time periods of other measurements shown in this manuscript indicated by the figure number.

empirical, and numerical models [*Anderson et al*., 2012]. The future of HAB forecasting likely lies in the combined efforts of in situ monitoring linked efficiently with sophisticated data assimilative models along with clear information dissemination [*Jochens et al*., 2010; *Franks*, 1997].

In the PNW, there are two known hot spots for *Pn* HAB formation: the Juan de Fuca Eddy, which forms above the Juan de Fuca Canyon at the western entrance to the Juan de Fuca Strait [*Hickey and Banas*, 2003; *Trainer et al*., 2002, 2009; *MacFadyen et al*., 2008], and Heceta Bank [*Hickey and Banas*, 2003; *Trainer et al*., 2001; *Hickey et al*., 2013] (Figure 1). Although the complete mechanism initiating toxin production is not fully characterized, both of these regions exhibit at least two features that are commonly associated with algal blooms: high nutrient supplies and retentive circulation [*Marchetti et al*., 2004; *Trainer et al*., 2009]. Transport from both of these *Pn* HAB hot spots to the coast is driven by the surface currents, which in the

© 2014. American Geophysical Union. All Rights Reserved.

PNW are dominated by elements of the California Current System (CCS) and local upwelling/downwelling winds.

In the CCS, near-surface southward seasonal mean transport is present over the mid to outer shelf in summer, and northward flow is present in fall and winter. Currents over the shelf and slope are dominated by the effects of local and remote wind stress, tides, and freshwater input. In the PNW, local winds are seasonal: northward during the winter months, southward during the summer/fall months with the northward winds being stronger and the southward winds weaker compared to those further south in the CCS [*Hickey*, 1979, 1989; *Hickey and Banas*, 2008]. Northward winds are downwelling favorable driving northward and onshore near-surface currents over the shelf (the latter due to Ekman transport). Southward winds are upwelling favorable driving southward and offshore near-surface currents over the shelf. Upwelling favorable winds drive coastal upwelling, which brings deep (cold, salty, nutrient rich, and oxygen poor) water near the surface at the coast. The transition to upwelling typically occurs during spring (the "spring transition"); however, the exact timing varies from year to year [*Huyer et al*., 1979; *Holt and Mantua*, 2009]. At depth, over the slope during the upwelling season, the California Undercurrent (CUC) flows northward providing the source waters for upwelling [*Hickey*, 1979; *Connolly and Hickey*, 2014]. During winter, the CUC is replaced by the northward Davidson current, which extends to the water surface. Other important physical processes in the PNW include coastal-trapped waves [*Battisti and Hickey*, 1984] and freshwater plumes [*Hickey et al*., 2009]. All of these processes are important in determining the formation and fate of HABs.

At least one clear transport pathway from the Juan de Fuca Eddy region to the coast has been described by *MacFadyen and Hickey* [2010] and *MacFadyen et al*. [2005] and is driven by the local surface currents: upwelling winds allow escape from the Eddy, subsequent downwelling winds bring particles to the coast. Although this particular transport mechanism has been well documented, it cannot account for all of the observed coastal *Pn* HAB events. Thus, other mechanisms must exist such as transport from a southern source, Heceta Bank, as shown by *Hickey et al*. [2013].

Freshwater plumes in the PNW have been suggested as an influence on transport pathways to the coast [*Thomson et al*., 1989; *Hickey et al*., 2009] and a potential influence on HAB transport from hot spots [*Hickey et al*., 2005]. The Columbia River (CR) plume is often bidirectional with plume water present north of the river mouth along the Washington (WA) coast and south of the river mouth offshore of the Oregon (OR) coast [*Hickey et al*., 2005, 2009; *Burla et al*., 2010; *Liu et al*., 2009a]. Furthermore, a significantly diluted freshwater plume from the Juan de Fuca Strait influences the Eddy region and interacts with the CR plume [*Hickey et al*., 2009]. Previous studies in the vicinity of the CR plume have suggested that the plume acts as a barrier to onshore and alongshore transport [*Hickey et al*., 2005; *Banas et al*., 2009a]. It is unknown whether the plume has a similar barrier effect on particles transiting from these hot spots on seasonal and interannual time scales. Additionally, observations in 2002 found onshore transport of *Pn* within low salinity CR plume water during storms suggesting the potential importance of plume entrainment [*Adams et al*., 2006].

As part of the PNWTOX (PNW TOXins) project working to improve our understanding of HABs in the PNW, here we use numerical simulations to predict transport pathways for *Pn* HABs in the PNW from two known source regions, the Juan de Fuca Eddy and Heceta Bank, to the coast. Our results are directed towards *Pn* specifically; however, the transport pathways apply more generally to any HAB species or even other near-surface particles originating from the chosen hot spots. In section 2, we describe the methods, which include realistic hindcast numerical simulations and particle tracking. In section 3, we discuss transport pathways from these known source regions in comparison with beach-based observations of *Pn* cell counts (section 3.1) and specifically address the influence of the CR plume (section 3.2). In the discussion (section 4), we propose a wind-intermittency index to describe the northern source transport pathway (section 4.1) and we employ a coupled biogeochemical model to improve *Pn* HAB predictability (section 4.2). Our findings are summarized in section 5. We find that transport pathways to the WA coast are seasonal, originating from the northern Juan de Fuca Eddy during the late spring, fall, and summer and from the southern Heceta Bank during the winter and early spring due to the seasonal large-scale upwelling/downwelling conditions. Transport from the Eddy requires wind relaxations and thus years with more frequent relaxations/downwelling during the upwelling season have more transport pathways to the coast. Overall the CR plume acts to block onshore transport, thus mitigating HAB beach events. In the alongshore direction, the CR influence is variable, sometimes blocking alongshore transport, sometimes enhancing alongshore transport. The latter is particularly important in transport from a southern source when entrainment allows for enhanced

© 2014. American Geophysical Union. All Rights Reserved.

alongshore transport. Overall, results are consistent with observed *Pn* HAB beach events and incorporating a biogeochemical model reduces false positives.

2. Methods

The results presented here utilize realistic hindcast numerical simulations and particle tracking experiments for 4 years, 2004–2007. After describing our numerical methods, we describe the model validation with an extensive suite of in situ observations.

2.1. Numerical Simulations

The numerical simulations of the PNW region are built with a framework developed by the University of Washington Coastal Modeling Group (UWCMG) [*MacCready et al*., 2009; *Liu et al*., 2009a, 2009b; *Banas et al*., 2009a, 2009b; *Sutherland et al*., 2011]. This modeling framework employs the Regional Ocean Modeling System (ROMS) [*Shchepetkin and McWilliams*, 2005], a free surface, hydrostatic, primitive equation model. The models are forced with realistic atmospheric forcing, tides, river flow, and boundary conditions to conduct hindcast simulations of the hydrodynamic conditions throughout the domain. The model domain and forcing described here (the "Cascadia" model) are similar to the Modeling of the Salish Sea (MoSSea) simulations [*Sutherland et al*., 2011]; however, resolution is focused on the coast rather than the inland waters and the domain extends farther offshore and farther south.

The Cascadia domain encompasses the inland waters of the Salish Sea (which includes Puget Sound, the Strait of Georgia, and the Juan de Fuca Strait) and the coastal ocean and estuaries of WA, OR, and Vancouver Island (VI), British Columbia (see Figure 1). The horizontal resolution ranges from 1.5 km at the coast to 4.5 km far offshore. The model has 40 S-coordinate layers with stretching parameters chosen to enhance resolution near the bed and in the upper water column ($\theta_s = 4$, $\theta_b = 0.8$, $h_c = 0$, Figures 1b and 1c). Grids with higher resolution performed comparably. The final simulations were run with the addition of a biogeochemical model (NPZDO) (see Davis et al., manuscript in preparation, 2014; Siedlecki et al., manuscript in preparation, 2014), five passive tracers, and diagnostics. Additional simulation details including forcing fields and boundary conditions are described in Appendix A. Figures 1d and 1e include the river flow and winds over the full 4 years of simulation for reference. Example snapshots of simulated surface salinity and temperature during the upwelling season are shown in Figure 2.

2.2. Particle Tracking

We employ a previously described particle tracking code [*Banas et al*., 2009b] that includes the option to surface trap particles (representing a buoyant particle) or to allow vertical excursions. Particles with vertical motion include advection due to the 3-D current field plus vertical mixing parameterized by a random displacement model [*North et al*., 2008; *Visser*, 1997].

Particles are released at the surface from the known regions of *Pn* HAB formation, the northern Juan de Fuca Eddy and the southern Heceta Bank sources, in a box of 31 $\times$ 31 particles spaced 2 km apart (Figure 1) and then tracked for 30 days. This "experiment" is repeated every 2 days. Both 2-D and 3-D particle tracking were tested and compared. Additionally, the number of particles, frequency of particle release, particle spacing, and length of tracking period were tested to ensure repeatability. From our numerous tests, we concluded that surface trapped particles released at intervals $<$5 days and spaced $<$10 km apart sufficiently resolve the synoptic variability and necessary spatial scales of interest. Live *Pn* cells are slightly positivity buoyant thus corroborating the use of surface-trapped particles. Finally, for most results in this paper, we use the first 15 days of particle tracking to approximate the lifetime of a PNW *Pn* bloom (2–3 weeks) [*Trainer and Suddleson*, 2005] and to encompass longer than twice the event time scale in the region ($\sim$3–5 days) [*Hickey*, 1979]. Example particle tracks are shown in Figure 2a during a 14 day period of upwelling followed by downwelling favorable winds (see Figure 2c).

2.3. Model Validation

The UWCMG has run several Cascadia models at different grid resolutions and completed extensive parameter testing and model validation. Here we present validation of the final Cascadia grid utilizing in situ hydrodynamic observations, satellite data, and glider data including time series as well as validation of important regional features. There are numerous features and processes that are important to the formation

© 2014. American Geophysical Union. All Rights Reserved.

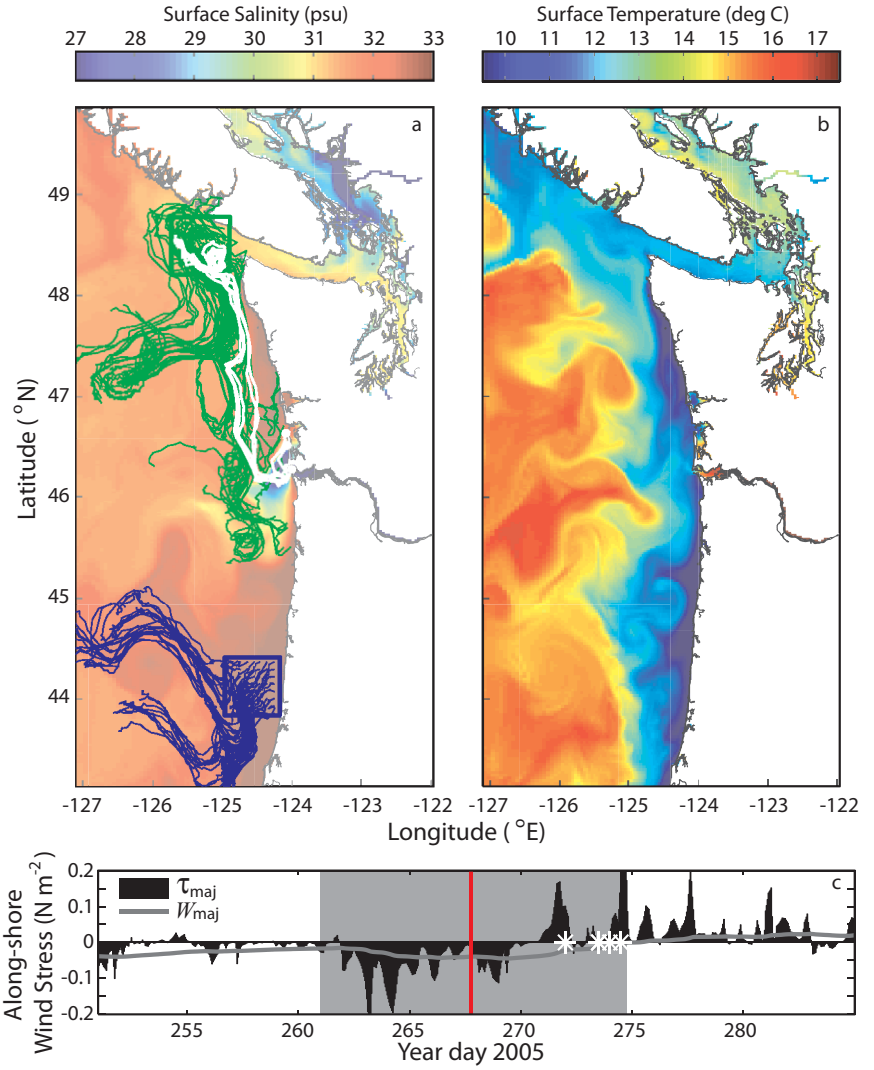

Figure 2. Model surface fields and particle tracks during upwelling season. Simulation snapshots of (a) sea surface salinity and (b) temperature on 26 September 2005 (red line in Figure 2c) are shown in the top plots. Particle tracks included in Figure 2a show 7% of the total particles (64 of the 961 particles from each release location) released on 19 September 2005 and tracked for 14 days. Particles released from the Juan de Fuca Eddy are in green; particles released from Heceta Bank are in blue. Any particles that beach at Long Beach, WA during this time period are in white and their beach landing times are marked as white stars in Figure 2c. Hourly alongshore wind stress (black) and their 8 day weighted average (gray). The vertical gray band marks the particle tracking period, the red line marks the time of the surface salinity and temperature fields. See Figures 1d and 1e, band 2 for context in the overall winds (end of upwelling season) and river flow (relatively low).

and transport of algal blooms in the PNW. Of particular interest are coastal-trapped waves, the regional upwelling, the CR plume, the aforementioned retentive circulation hot spots, and the CUC. Overall, our model exhibits high skill and successfully reproduces these important features of PNW coastal oceanography.

2.3.1. Overall Model Skill

Model currents, salinity, and temperature are validated using an extensive array of observations (see Figure 1 and more details in Appendix A). Mooring records were provided from the Ecology and Oceanography of Harmful Algal Blooms—Pacific NorthWest (ECOHAB-PNW) and River Influences on Shelf Ecosystems (RISE) projects (May–September 2004–2007) as well as the Canadian Institute of Ocean Sciences (IOS) (year-round). Moorings had acoustic Doppler current profilers (ADCPs) and conductivity, temperature, depth sensors (CTDs), or temperature sensors at varying depths. NOAA tide gauges (http://tidesandcurrents.noaa.gov/) were used to validate sea surface height. Finally, CTD casts throughout the domain were used to test the

© 2014. American Geophysical Union. All Rights Reserved.

Table 1. Final Model Willmott Scores[a]

a	A1	J2C	EH1	EH3	EH2	EH4	RN	RC	RS	RR	Average	Casts
U_{minor}	0.38	0.36	0.69	0.7	0.6	0.6	0.54	0.63	0.51		0.58	
U_{major}	0.58	0.71	0.94	0.81	0.85	0.8	0.66	0.73	0.84		0.77	
S	0.24		0.65	0.56	0.88	0.63	0.84	0.79	0.86	0.52	0.66	0.92
T	0.49		0.56	0.6	0.88	0.9	0.87	0.85	0.89	0.91	0.77	0.97
$<U_{min}>$	0.37	0.51	0.63	0.45	0.56	0.52	0.46	0.59	0.51		0.51	
$<U_{maj}>$	0.58	0.79	0.83	0.77	0.93	0.89	0.74	0.75	0.87		0.79	
$<S>$	0.24		0.65	0.57	0.9	0.62	0.88	0.85	0.9	0.54	0.68	
$<T>$	0.48		0.55	0.6	0.92	0.91	0.9	0.88	0.93	0.92	0.79	

b	Charleston 1	So. Beach 2	Garibaldi 3	Astoria 4	La Push 5	Neah Bay 6	Port Ang. 7	Port Town 8	Friday Har. 9	Cherry Pt. 10	Seattle 11	Tacoma 12	Average
η	0.95	0.97	0.99	0.96	0.99	0.99	0.98	0.96	0.98	0.98	0.93	0.93	0.97
$<\eta>$	0.82	0.89	0.85	0.94	0.92	0.92	0.91	0.86	0.84	0.86	0.85	0.83	0.87

[a]Willmott skill scores (*WS*) for the final Cascadia medium resolution model for 2005 (initialized with results from the end of the 2004 simulation). The various mooring locations and NOAA water level gauges are marked in Figure 1. (a) *WS* are included for the minor and major principal axes velocity components (determined from the subtidal time series), salinity, and temperature for the hourly and subtidal (with brackets, $< >$) time series over all time and depths that the observations exist. *WS* for all of the CTD casts combined are in the last column of a. b) Both hourly and subtidal water level is compared over the full year from NOAA gauges. Gauges are listed from south to north along the coast followed by increasing distance into the Salish Sea. Port Angeles and Port Townsend are in the Juan de Fuca Strait, Friday Harbor and Cherry Point are in the Strait of Georgia, and Seattle and Tacoma are in Puget Sound. See the associated locations by number in Figure 2.

vertical distribution of temperature and salinity. These included casts from the spatially comprehensive ECOHAB-PNW [*MacFadyen et al*., 2008] and RISE [*Hickey et al*., 2010] projects as well as the Puget Sound Regional Synthesis Model (PRISM), Washington State Department of Ecology, the Joint Effort to Monitor the Strait (JEMS), and IOS totaling over 7000 CTD casts from 2004 to 2007. Note that casts span the entire year, although the majority of the open coast casts were taken during the upwelling season.

We utilized three different model skill metrics to assess the simulation performance and test different model setups: the Skill Score (*SS*) [*Murphy*, 1988], Willmott Skill Score (*WS*) [*Willmott*, 1982], and correlation coefficient (*r*), discussed in more depth in *Liu et al*. [2009b], *Sutherland et al*. [2011], and Appendix A. Skill analyses of various model setups are described in Appendix A, while *WS*s for the final simulations during 2005 are shown in Table 1. *WS*s are computed on the minor and major velocity components defined by principal axes analysis as well as on the hourly and subtidal (Godin low pass filter) [*Emery and Thomson*, 2004] time series using all available observational data. Average *WS*s are strong (Table 1, 1 indicates perfect agreement, 0 complete disagreement), particularly for the major principal axes velocity component and temperature. Salinity agreement is weaker because of a salinity bias that is inherited from the NCOM boundary conditions [*Liu et al*., 2009b; *Sutherland et al*., 2011]. *WS*s are lowest (worst) beyond the shelf break (A1 and EH3) and highest (best) on the shelf (EH2, EH4, RN, RC, and RS). Overall *WS*s for the salinity and temperature from all of the 2264 CTD casts in 2005 (see Figure 1) are high ($\geq$0.92, Table 1a, far right-hand column) as are *WS*s for sea surface elevation (Table 1b). Additional details on Table 1 are given in Appendix A.

Because the data are unevenly sampled in time and space, these average *WS*s may obscure or bias some processes. For example, fewer winter data means these *WS*s are biased toward summertime upwelling processes. Thus, we have also examined *SS*, *WS*, *r*, and comparison plots over time and space separately (not all included here) and observe consistent model skill. For example, the model captures both the tidal and event-scale variability (see Figures 3 and 4) as well as the vertical structure of velocity, salinity, and temperature (see the right-hand columns of Figures 3 and 4). Additionally, event scale and seasonal variation in the velocity, salinity, and temperature indicate the model is successfully reproducing coastal-trapped waves, coastal upwelling, and CR plume movements as described below.

2.3.2. Coastal-Trapped Waves

Coastal-trapped waves (CTWs) propagate up the OR and WA coastline primarily as a result of wind forcing off northern CA [*Battisti and Hickey*, 1984]. These waves directly influence the velocity structure over the shelf, including the surface velocity, as they drive strong ($\sim$0.15 m s^{-1}) quasi-barotropic velocity fluctuations on time periods of 5–10 days [*Battisti and Hickey*, 1984]. Additionally, they influence the alongshore pressure gradient over the slope and thus the CUC [*Connolly et al*., 2014]. The event-scale variability in velocity structure over the midshelf mooring, RS (Figure 4), shows that our model is properly propagating CTWs from the boundaries. Figure 4 includes the subtidal along-stream velocity both at the surface and at 30 m depth where the signature of the CTWs will dominate the variance. Despite their dominance at depth,

© 2014. American Geophysical Union. All Rights Reserved.

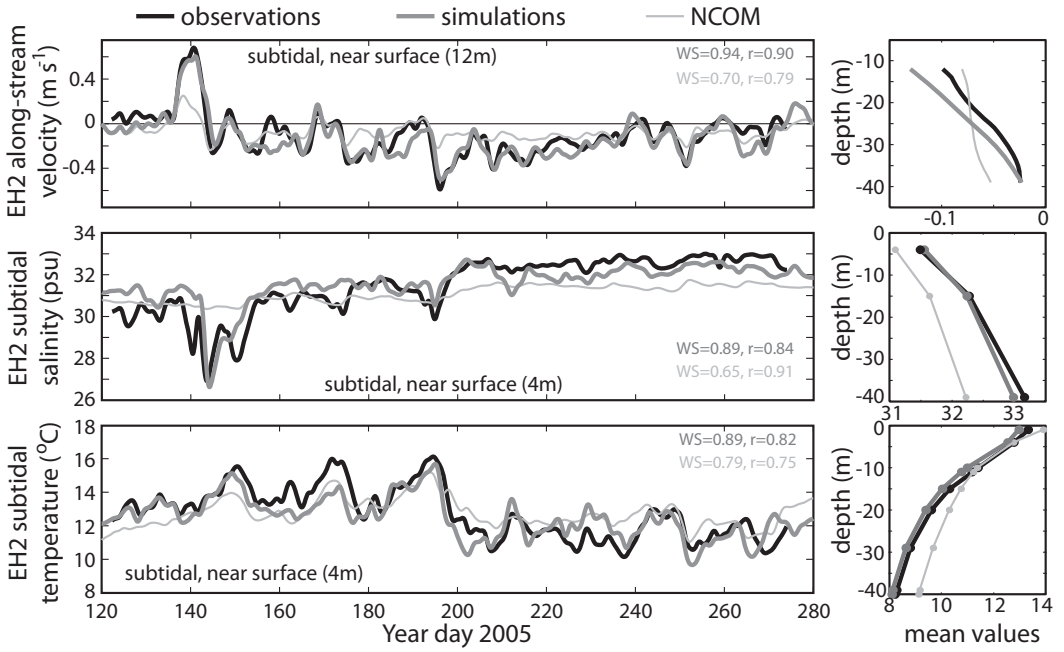

Figure 3. Modeled and observed near-surface subtidal velocity, salinity, and temperature at EH2. (left) Subtidal time series near the water surface and (right) residual mean profiles over the period of observations for (top) along-stream velocity, (middle) salinity, and (bottom) temperature at EH2, an ECOHAB-PNW mooring, in 46 m of water (see Figure 1). Observations are in black, model results are in gray, and NCOM results are in thin light gray. Willmott skill scores (*WS*) and correlation coefficient (*r*) are included in the left plots for the near-surface subtidal time series. Figures 1d and 1e show the river flow and 8 day weighted winds during this time period marked in the lightest gray and labeled 3–4.

CTWs play an important role in the surface velocity fields, which impact HAB transport, as seen in the strong correspondence between Figures 4a and 4b.

2.3.3. Coastal Upwelling/Downwelling

Satellite images are used to compare mean monthly sea-surface temperature (SST) with our simulations during 2005. Satellite data are from MODIS Aqua (version R2012.0), provided by the NASA Ocean Biology Processing Group. The 4 km daily global imagery was subset to the US west coast (25–50°N, 110–135°W) prior to cloud-clearing and temporal binning. The daily imagery for each year was processed using DINEOF version 2.2 [*Beckers and Rixen*, 2003]. The reconstructed data were then subset to the PNW region and temporally binned to monthly averages using an arithmetic mean. Figure 5 presents monthly means of SST from the satellite and simulations every 3 months beginning in February 2005.

Seasonal sea surface warming is well captured ranging from ~8°C in January to ~18°C in August. The coastal upwelling signal of nearshore cold water begins in June and reaches a maximum in August, disappearing in November. Enhanced upwelling just south of Quillayute Point and over Heceta Bank is captured in the simulations, although the WA shelf upwelled water is slightly too cold (~0.5–1°C, see Figures 5c and 5g). The surface currents (Figures 3a and 4a) and sea surface height (not shown) show the clear upwelling/downwelling seasonal patterns, with flow toward the north and high sea level at the coast during the winter downwelling months switching to flow toward the south and low coastal sea level during upwelling months.

2.3.4. Columbia River Plume

Signatures of the CR plume presence can be seen in many of the data sets, confirming that our model represents the salinity, temperature, and variability of the plume structure. Nearshore, the CR plume is seen during the winter months as a slightly colder signal north of the CR mouth (see Figures 5a and 5e) to a warmer than background signal in May both north and south of the mouth (see Figures 5b and 5f). During periods of downwelling favorable winds, the plume hugs the Washington coast and is observed at moorings north of the CR mouth. For example, near day 140 in Figure 3, strong downwelling winds lead to northern near-surface flow (Figure 3a) followed by a sharp decrease in salinity (Figure 3b) as the plume passes over the EH2 mooring. During upwelling favorable winds, the plume moves offshore and southward (e.g., Figure 2a), resulting in decreased salinities south of the CR mouth such as seen near day 160 at the RS mooring (Figure 4b).

© 2014. American Geophysical Union. All Rights Reserved.

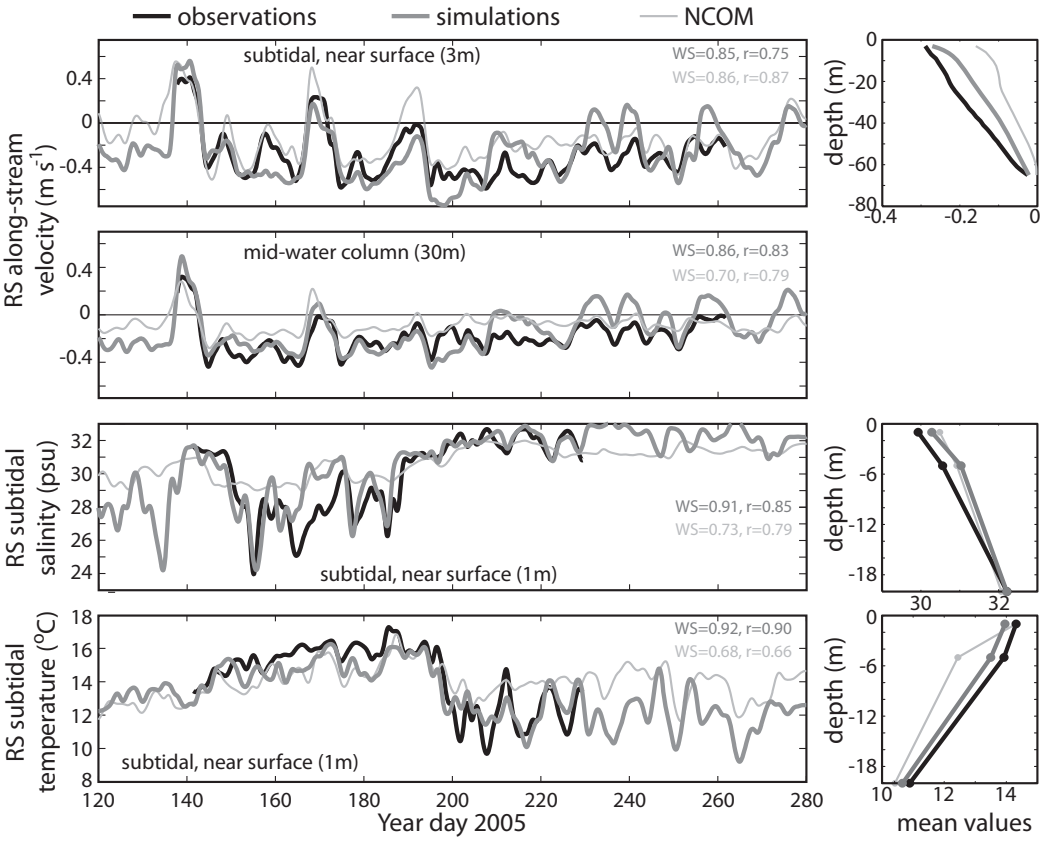

Figure 4. Modeled and observed near-surface subtidal velocity, salinity, and temperature at RS. Similar to Figure 3 but for the RISE South mooring (RS) which is in ~73 m of water (see Figure 1). An additional plot (second plot from top) is the midwater column along-stream velocity at 30 m depth.

2.3.5. Regional *Pn* HAB Hot Spots

2.3.5.1. Juan De Fuca Eddy

The Juan de Fuca Eddy, a semiretentive feature near the mouth of Juan de Fuca Strait [*Tully*, 1941; *Denman and Freeland*, 1985], plays a large role in *Pn* HAB formation and transport [*Trainer et al*., 2002, 2009; *Hickey and Banas*, 2003; *MacFadyen et al*., 2005, 2008]. This cyclonic, cold-core eddy persists throughout much of the summer and fall. Unfortunately, the cold signal of the Juan de Fuca Eddy and Juan de Fuca Strait in the summer months is too warm in model results (Figures 5c and 5g). This is a known model deficiency: the SST exiting the Salish Sea is high by ~2°C. This offset decreases with depth, disappearing by ~20 m beneath the surface. We believe this may be due to insufficient mixing within the Salish Sea and Juan de Fuca Strait where our model resolution cannot resolve the extreme bathymetry. Despite this near-surface deficiency, the Juan de Fuca Strait estuarine exchange flow and Eddy are consistent with observations at depth; e.g., see Figure 6, which shows the observed and measured salinity and temperature at 35 m depth during a September 2005 ECOHAB-PNW cruise. The Juan de Fuca Eddy is apparent as a region of higher salinity and lower temperature and the observations and model are consistent in terms of eddy size, extent, salinity, and temperature. The eddy development in our model is consistent with prior model studies by both *MacFadyen and Hickey* [2010] and *Foreman et al*. [2008] that show that the Eddy begins as enhanced upwelling off of Cape Flattery (near tide gauge #6, Figure 1), which spreads westward and is periodically renewed during upwelling periods.

Particle tracking experiments were used to examine the Eddy circulation. Particles released in the Eddy region become trapped in the Eddy, circulate cyclonically during downwelling winds, and can escape the Eddy to the south into the WA shelf upwelling jet during upwelling (e.g., see the particle tracks in Figure 2a). This relationship between the eddy retention time and the winds (eddy is retentive during downwelling winds and "leaky" during upwelling winds) is consistent with previous observations [*MacFadyen et al*., 2005, 2008] and models [*MacFadyen and Hickey*, 2010]. Particles released in the Eddy region can remain in the Eddy for up to the full tracking period

© 2014. American Geophysical Union. All Rights Reserved.

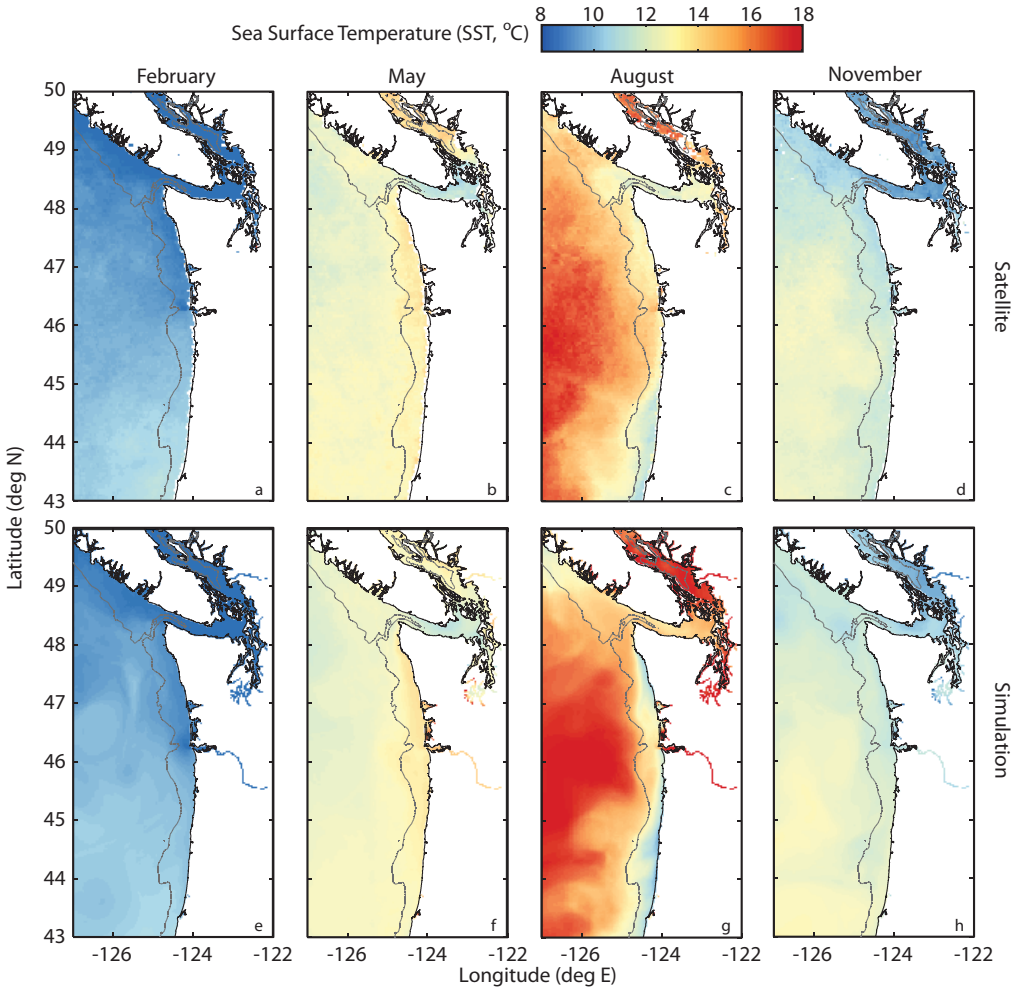

Figure 5. Mean Monthly SST comparisons. (a–d) Satellite derived mean monthly SST. (e–h) Simulation mean monthly SST. Every third month starting in February 2005 as labeled is included. The gray bathymetry contour is at 200 m. Figures 1d and 1e indicate the monthly averaged periods with dashed vertical bars.

(30 days) but on average are retained ~10 days, similar to physical drifter observations [*MacFadyen et al.*, 2005]. Additionally, features surrounding the Eddy are consistent with observations including the Vancouver Island Coastal Current (VICC) and the Juan de Fuca Strait Exchange flow. The VICC flows from the Juan de Fuca Strait along VI to the northwest [e.g., *Tully*, 1941; *Hickey et al.*, 1991] sometimes wrapping around the Eddy (e.g., Figure 2). The Juan de Fuca Strait exchange flow (measured at moorings EH1 and J2C) exhibits estuarine exchange that can reverse during strong downwelling favorable winds [*Hickey et al.*, 1991; *Hickey*, 1989; *Thomson et al.*, 2007]. These features interact with the Eddy and influence its strength.

2.3.5.2. Heceta Bank

Heceta Bank is a hot spot for high productivity [*Venegas et al.*, 2008; *Kim and Barth*, 2011; *Rivas and Samelson*, 2011] and specifically a known hot spot for *Pn* bloom formation [*Trainer et al.*, 2001; *Hickey and Banas*, 2003; *Hickey et al.*, 2013]. Our model captures the enhanced upwelling over Heceta Bank, the separation of the upwelling jet offshore [*Castelao and Barth*, 2006; *Kosro*, 2005], and the retentive recirculation over the bank inshore of the separated jet [*Kirincich and Barth*, 2009; *Whitney and Allen*, 2009] (see Figures 5c and 5g, for an example). The high retention is observed in particle tracking results in which particles remain over the bank for extended periods of time.

2.3.6. California Undercurrent

The CUC is a large-scale feature that forms over the midlatitude Eastern Pacific Ocean continental slope [*Hickey*, 1979] extending as far north as VI [*Thomson and Krassovski*, 2010; *Pierce et al.*, 2000]. In the northern CCS, the CUC has been linked to the alongshore pressure gradient [*Hickey*, 1979, 1998; *Werner and Hickey*,

© 2014. American Geophysical Union. All Rights Reserved.

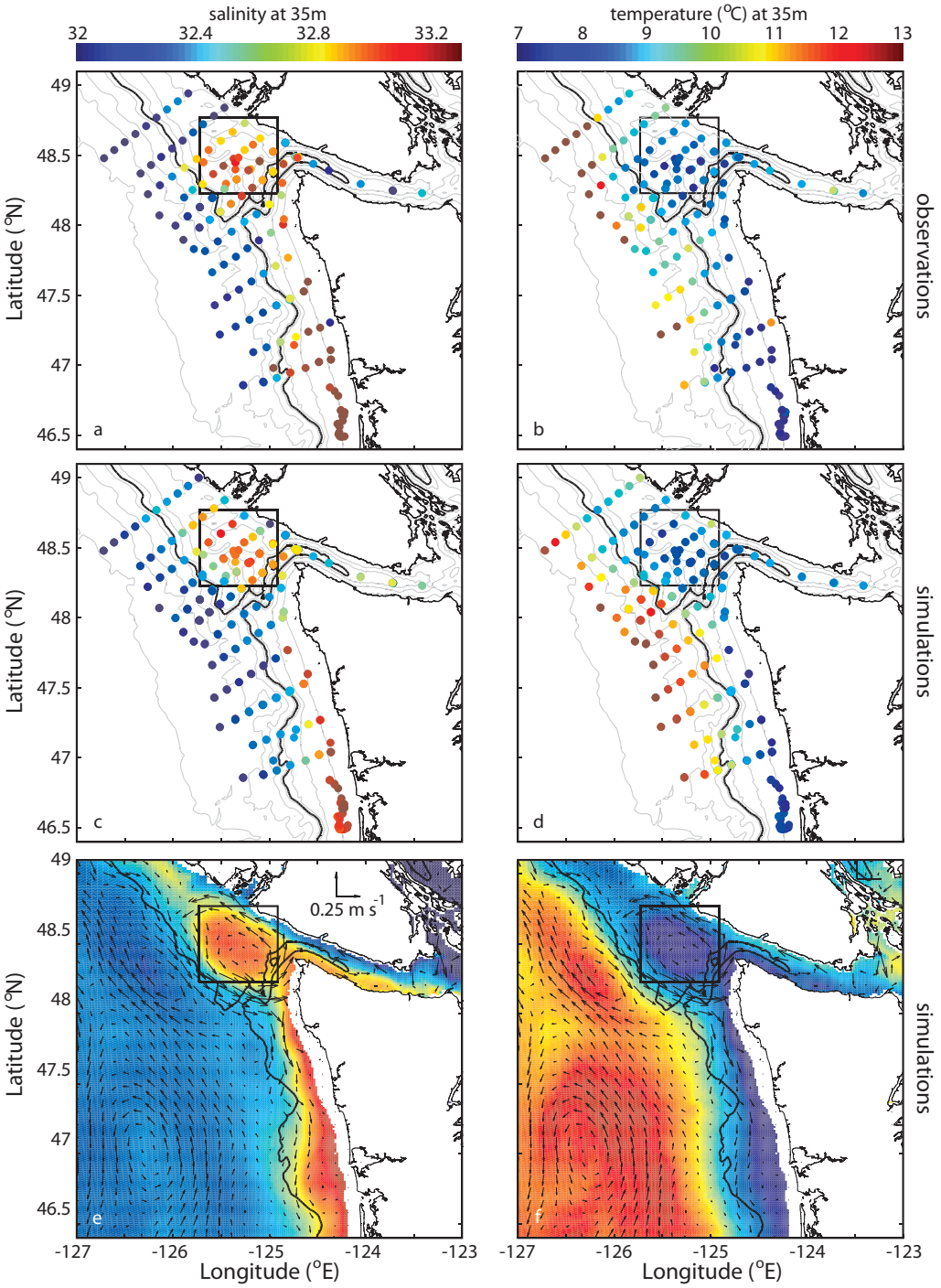

Figure 6. Juan de Fuca Eddy upwelling at 35 m depth. (a) CTD salinity observations and (b) CTD temperature observations at 35 m depth taken over the time period from 5 to 21 September 2005 during the ECOHAB-PNW project. Figures 1d and 1e show the river flow and 8 day weighted winds during this upwelling favorable time period (green bar 6). (c) Simulated salinity and (d) simulated temperature at 35 m at the same time and space as the observations. (e) Simulated salinity and (f) simulated temperature time averaged over the same time period as the observations. Note that because of a bias in the deep salinity inherited from the NCOM Global model, the simulated salinity is offset by 0.2 psu (from 32 to 32.2) but covers the same range. Thin arrows show velocity at 35 m depth regridded onto a regular horizontal grid. The box around the Eddy shows the Eddy-influenced region where the particles are released in the particle tracking experiments. Depth contours are 50, 100, 150, 250, 500, 1000, and 2000 m and the thick contour is 200 m.

© 2014. American Geophysical Union. All Rights Reserved.

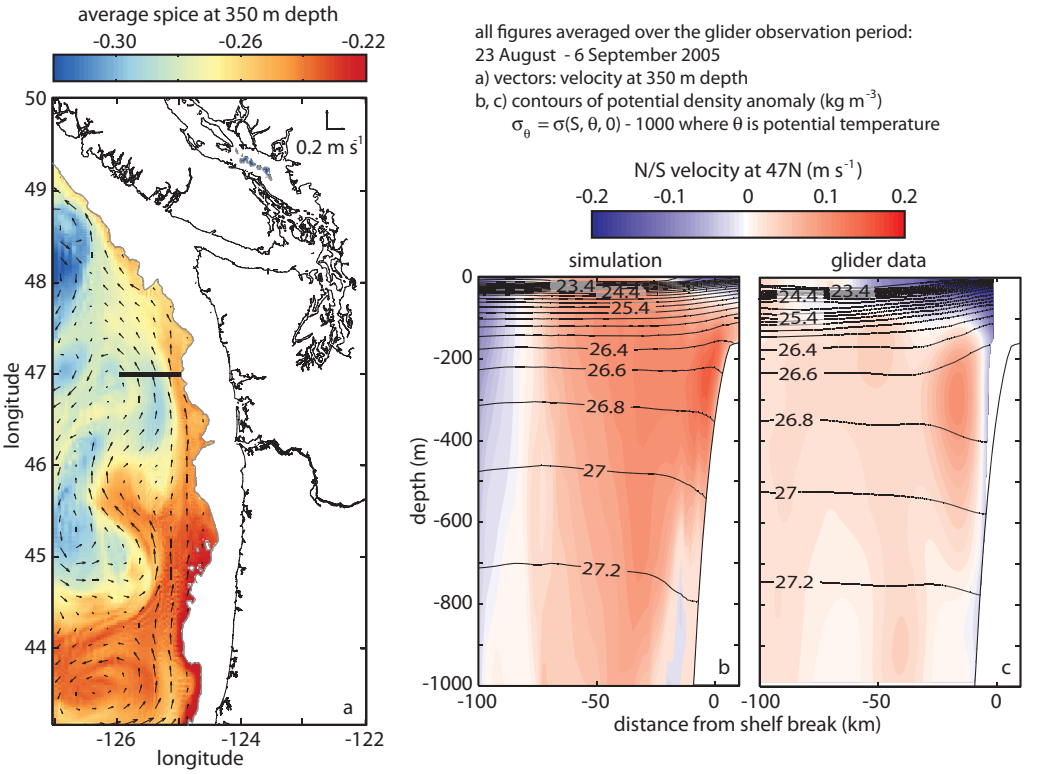

Figure 7. California Undercurrent validation. (a) Model spice (color) and velocity vectors (arrows) at 350 m depth. (b) Model cross section at 47°N (see line in Figure 7a) of north-south velocity (color scale) and contours of potential density. (c) Observed cross section at 47°N from the glider with contours of potential density and computed geostrophic north-south velocity. All plots are averaged over the transit time period of the glider, 23 August to 6 September 2005. Figures 1d and 1e show the river flow and 8 day weighted winds during this upwelling favorable time period (red bar 7).

1983; *Connolly et al*., 2014]. It typically manifests itself as a depth-intensified northward current centered below the shelf-break (∼250–350 m) and is present throughout the summer/fall upwelling season. The CUC plays an important role in determining the water properties, source depth, and chemistry of upwelled water [*MacFadyen et al*., 2008; *Connolly and Hickey*, 2014; Siedlecki et al., manuscript in preparation 2014], thus impacting phytoplankton blooms. CUC water derives from the tropics and thus is relatively high in both temperature and salinity [i.e., high "spice," *Flament*, 2002]. It also contains high nutrients and low dissolved oxygen [*Lynn et al*., 2003; *Hickey*, 1979].

Glider cross sections of density and geostrophic velocity [*Pelland et al*., 2013] have been used to evaluate the placement, strength, and variability of the CUC in our simulations (e.g., Figure 7). The CUC is identified as a northward velocity core centered below the shelf break in both the observations and model. Comparisons to 20 glider transects throughout 2005–2006 (not shown) show that the model consistently generates a CUC and that its magnitude, location, and seasonal development are in good qualitative agreement with the observations.

3. Results

3.1. Potential HAB Transport Pathways

Potential HAB surface transport pathways originating from the two hot spots are determined from the particle tracking experiments described in section 2.2. A particle "beaching" is defined as passing within the 30 m isobath of a defined latitudinal extent. Shoreward of the 30 m isobath is chosen to approximately demarcate the seaward extent of the innershelf, where the upper and lower boundary layers intersect [*Lentz and Fewings*, 2012]. Our model excludes some innershelf physical processes, such as surface waves, that could impact whether particles actually reach the beach. Sensitivity tests using the 20, 10, and 4 m isobaths as "beaching" cut offs (rather than 30 m), resulted in similar temporal patterns but fewer total beachings (up to 60% fewer). White lines in Figure 2a show typical beach landing pathways on a map view during upwelling winds.

© 2014. American Geophysical Union. All Rights Reserved.

Particles released and tracked over our 4 year simulations show clear seasonal variation in transport pathways from the potential source regions based on the predominant wind direction. Figure 8 shows particle paths (latitude versus time) for only those particles that reach Long Beach, WA (Figure 1) within 15 days of release from either the Eddy or Heceta Bank (thus showing only a portion of the total particles that were released every 2 days throughout the 4 years). In general, during the upwelling summer and fall months, particles move from the source regions southward in the coastal jet and offshore; during the winter and spring months they tend to move northward over the innershelf and onshore following the large-scale wind-driven surface currents. This means that for WA beaches, particles from the Juan de Fuca Eddy region can reach the beach during the summer/fall while particles from the Heceta Bank region can reach the beach during the winter/spring as seen in Figure 8, consistent with observations [e.g., *MacFadyen et al*., 2005; *Hickey et al*., 2013].

3.1.1. Summer/Fall *Pn* Events

During the time period examined (2004–2007), high *Pn* cell counts were observed during the summer/fall upwelling period every year at Long Beach, WA by the Olympic Regional Harmful Algal Bloom (ORHAB) program (Figure 8b). It is important to note that these high *Pn* cell count events did not always correspond to high DA concentrations. Each of these summer/fall events corresponds with particles arriving from the Juan de Fuca Eddy region (Figure 8a).

Wind patterns associated with these events are fairly consistent. Figures 9a and 9c show the mean winds (±1 standard deviation) for all beachings in 2005 where the *x* axis is in days relative to the beaching time. Winds are overall weakly upwelling favorable but on average relax and/or reverse to downwelling favorable just before the particle beaches. The upwelling favorable winds allow escape from the Eddy and southern transport while the subsequent relaxation or downwelling drives onshore Ekman transport. This pattern of winds was identified by *MacFadyen et al*. [2005] and *MacFadyen and Hickey* [2010] as critical to this transport pathway. Very few particles take 15 days to reach the beach, over 50% of the particles beach within less than 10 days, and almost all beachings take at least 5 days from the Eddy (Figure 9e).

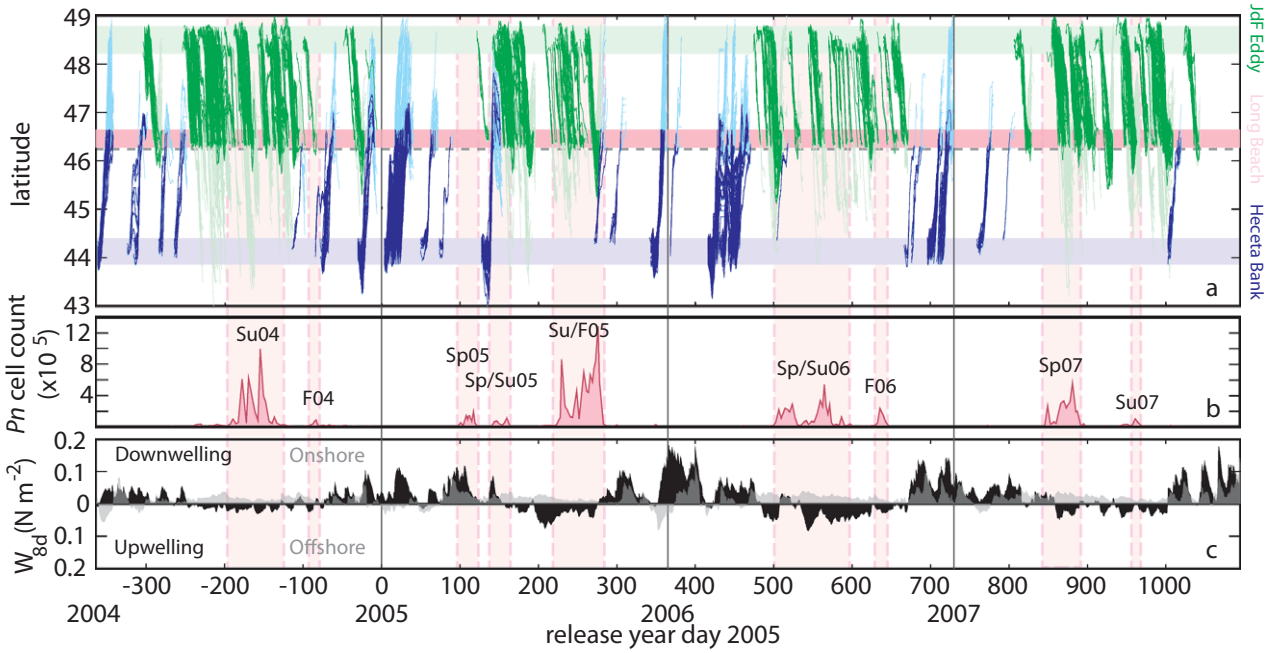

Figure 8. Particle tracking results. (a) The latitude of particles originating from both source regions (the Eddy is in green, Heceta Bank is in blue) and landing at Long Beach (pink) are plotted over time. The dashed gray line indicates the location of the CR mouth. Particles are released continuously throughout the year, however only those reaching the beach are plotted, thus time periods without lines indicate that no particles reached Long Beach. Each line is dark until the beaching occurs and then light thereafter as some particles reach the beach region and then subsequently escape. (b) *Pn* cell count at Long Beach, WA observed in the ORHAB sampling program. (c) 8 day cumulative weighted wind stress rotated into the principal axes directions where black indicates the along-shelf winds (positive is downwelling favorable) and gray shows cross-shelf winds (positive is onshore). Pink rectangles outline observed HAB beach events and are labeled as Spring (Sp), Summer (Su), or Fall (F) events.

© 2014. American Geophysical Union. All Rights Reserved.

3.1.2. Spring *Pn* Events

Spring/early summer events were observed in 2005, 2006, and 2007 (Figure 8b). The source of these cells depends on whether the spring transition has occurred or not. For example, in 2005, the spring transition was delayed [*Kosro et al*., 2006] and the late spring event (Sp/Su05 in Figure 8) was caused by transport from Heceta Bank. In 2006 and 2007 however, the spring events occurred after the spring transition and thus were due to transport from the Eddy (Sp/Su06 and Sp07 in Figure 8). The only spring event that is not captured with this model is the mid-spring 2005 event (Sp05 in Figure 8). This is likely a result of the sensitivity of this transport pathway to plume location, wind history, and particle release times as beachings from Heceta Bank occur one day earlier and our higher resolution model did identify this event with particles deriving from Heceta Bank. Additionally, *Hickey et al*. [2013] use observations to show this event is from a southern source near Heceta Bank originating on 20 March 2005. Our particle tracking releases are on 19 and 21 March, and the 19 March release results in the early landings seen in Figure 8. Thus, our model results are largely consistent with the spring transport pathway from a southern source onto the WA coast suggested by measurements [*Hickey et al*., 2013], although this transport pathway appears more sensitive to model resolution than the Eddy transport pathway as borne out by higher resolution model runs not shown here.

Spring events from the Heceta Bank region are associated with persistent downwelling winds that lead to both northward and onshore transport (see the average winds in Figures 9b and 9d). In many cases, particles from Heceta Bank do not travel as far north as the WA coast and, as we will describe in section 3.2, entrainment into the CR plume is an important aspect of this pathway. While this pathway results in fewer time periods with Long Beach landings (relative to the Eddy pathway), the pathway is robust, bringing significantly more particles to the beach per large event. Similar to Eddy beachings, very few particles take 15 days to reach the beach and over 50% of the particles beach within 10 days. Heceta Bank beachings can occur faster than Eddy beachings, in as few as 2.5 days when storm winds are sufficiently strong (see Figure 9f).

3.1.3. Interannual Variability

Significant interannual variability occurs in our 4 year modeling period. For example, 2004 and 2007 have weaker upwelling winds with intermittent relaxation/downwelling events (Figure 8c). The intermittent relaxation/downwelling winds allows more total particles to reach the coast during the upwelling season as seen by the higher number of beachings during the 2004 and 2007 upwelling seasons (O(10^4) particles, Figure 8a). Strong

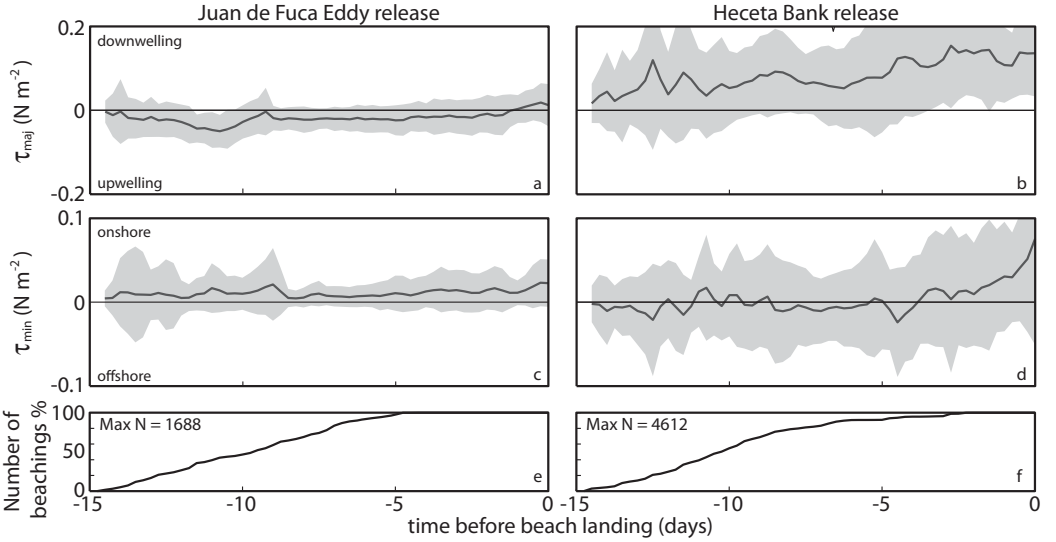

Figure 9. Mean winds during beach landings. Mean (a and b) alongshore and (c and d) cross-shore winds (solid line) ±1 standard deviation (gray bands) for all particles landing at Long Beach during 2005. (e and f) The percentage of total beachings over time. For example, the % at −10 days indicates the percentage of particles that take 10 days or longer to reach the beach. The *x* axis indicates time before the beaching, such that 0 days indicates the beaching time and −15 days indicates 15 days prior to beaching. The left plots (Figures 9a, 9c, and 9e) show the winds during landings from the northern source, the Juan de Fuca Eddy. The right plots (Figures 9b, 9d, and 9f) show the winds during landings from the southern source, Heceta Bank. Note that the vertical scale on the alongshore (major principal axis component) and cross-shore winds are different.

© 2014. American Geophysical Union. All Rights Reserved.

upwelling winds, as in late 2005 (late transition) and throughout the 2006 upwelling season, prevent particles from reaching the coast, as they are swept offshore resulting in fewer beachings (O(10^3) particles, Figure 8a).

Conversely, while the transport pathway from Heceta Bank varies substantially between years, there is no clear interannual trend. Intermediate strength, persistent downwelling winds appear to be most important in bringing particles from the Heceta Bank region to the WA coast (e.g., winter 2005 and spring 2006). Very strong downwelling winds do not contribute to WA beachings as particles either immediately beach on the OR coast, or in the case of CR plume entrainment, sweep further north in less time, reaching the VI shelf or the Salish Sea.

3.2. The Influence of the CR Plume

To specifically address the influence of the CR plume on these transport pathways, we compare the results from the above-described realistic hindcast simulations to simulations excluding the CR and the CR plume (No-CR simulation). This is accomplished by altering the model grid such that points within the CR are considered land, effectively shutting off the river at its mouth. The influence of the plume on onshore and alongshore transport applies to any particles following these transport pathways.

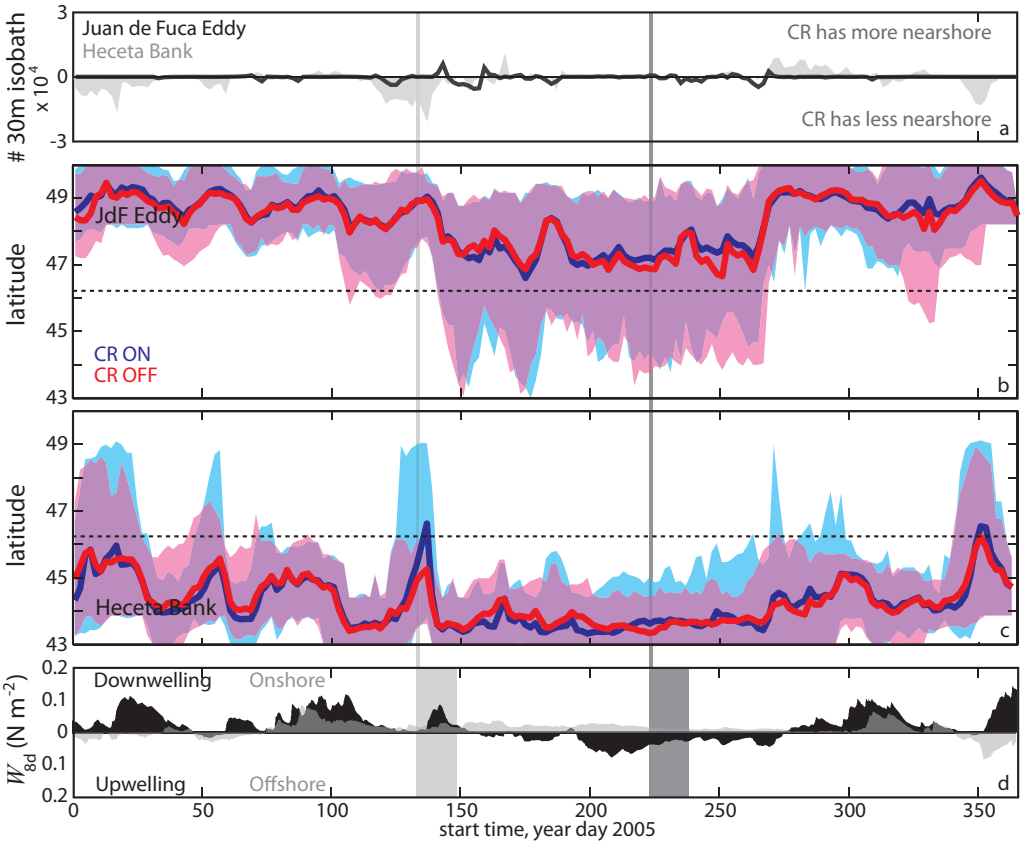

Figure 10. CR plume influence. (a) The difference in the number of particles originating from both source regions and landing within the 30 m isobath between the full simulation and No-CR experiments. Black indicates the northern Juan de Fuca Eddy source while gray is the Heceta Bank southern source. When these curves are less than zero, the full simulation (CR on) has fewer particles nearshore. (b) The mean latitudinal extent of the particles released from the Juan de Fuca Eddy region over time is shown as a line with the minimum and maximum latitudinal extent filled in. Blue colors are the full simulation while red colors are the No-CR experiments. The No-CR minimum and maximum spread (light blue) is semitransparent such that when the latitudinal extents overlap purple is seen. The CR mouth location is marked with a dashed line. (c) Same as Figure 10b, but for particles released from the Heceta Bank region. (d) 8 day cumulative weighted winds rotated into the principal axes directions where black is the along-shelf winds (positive is downwelling favorable) and the gray shows cross-shelf winds (positive is onshore). The vertical lines indicate the start time of the particle releases shown in Figure 11 while the bands show the full tracking period (light gray marks Figure 11a, dark gray marks Figure 11b).

© 2014. American Geophysical Union. All Rights Reserved.

3.2.1. CR Plume Influence on Onshore Transport

To examine the impact of the CR plume on onshore transport, we compare the number of particles that transit within the 30 m isobath along the entire OR/WA coastline between the full simulation and the No-CR simulation (Figure 10a). Typically, more particles beach in the No-CR simulation for both northern and southern sources (Figure 10a). Over the course of 1 year, the No-CR simulation allows 40% more beachings than the full simulation from the northern source and 13% more beachings from the southern source. This suggests that the CR plume frequently acts as a barrier to onshore transport, in agreement with previous studies [*Banas et al*., 2009a]. Effectively, the CR plume forms a convergence front that acts as a barrier to cross-frontal transport and thus onshore transport of surface particles starting offshore of the plume. During the transition to downwelling (necessary for onshore transport), strong vertical mixing leads to vertical isopycnals, thus shutting down cross-shelf transport within the plume [e.g., *Austin and Lentz*, 2002; *Rao et al*., 2011]. If the plume reaches the coast before the upwelling front, constituents previously trapped in or offshore of the upwelling front are blocked from reaching the coast [*Austin and Lentz*, 2002]. Long Beach sits well within the region where the CR reaches the coast first (~70–100 km from the CR mouth) [*Rao et al*., 2011]. Thus, this mechanism blocks onshore transport to the southern WA coast.

3.2.2. CR Plume Influence on Alongshore Transport

Banas et al. [2009a] suggested that the CR plume acts as a semipermeable along-coast barrier, reducing overall southward transport on the shelf. Although we do find individual events in which this effect on transport of particles from the northern source is clear (e.g., Figure 11b), the overall effect on the mean latitudinal distribution of particles after 15 days is minimal (Figure 10b, solid lines). Examining the full range of latitudinal particle distribution (shaded regions), some differences between the full simulation (dark gray shaded) and No-CR (light gray shaded) emerge, yet overall remain minimal.

Particles from the southern source similarly have minimal difference in the mean latitudinal extent (Figure 10c). However, particles from the southern source exhibit larger differences in their full latitudinal distribution with some particles transiting significantly further north (over 2° of latitude) in the full simulations than

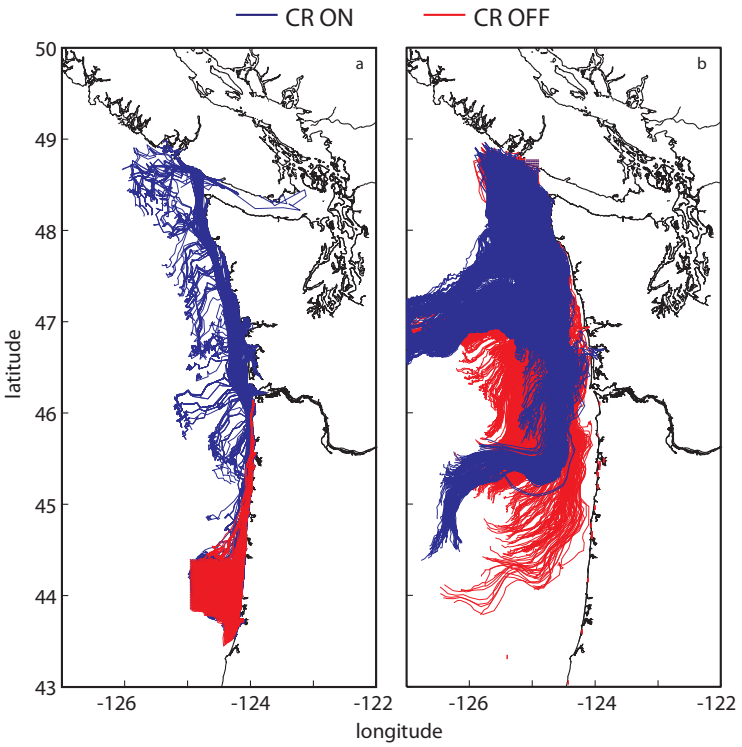

Figure 11. Snapshots of the CR plume influence on transport. Particle tracks over 15 days for the full simulation (blue) and No-CR experiment (red) from (a) the southern source during a period of entrainment and downwelling winds and from (b) the northern source during a period of upwelling favorable winds. Time stamps indicating these 15 day particle tracking windows are included in Figure 10. The start time is marked with a vertical line through all subplots, the 15 day tracking period is indicated as rectangles in Figure 10d.

© 2014. American Geophysical Union. All Rights Reserved.

in the No-CR simulations (Figure 10c, dark gray shaded versus light gray shaded). This enhanced northward transport occurs because particles are entrained into the CR plume, where onshore transport is blocked while alongshore transport is enhanced due to the buoyant coastal current [e.g., *Fong and Geyer*, 2002]. Figure 11a shows a clear example of the influence of plume entrainment during strong downwelling favorable winds. Thus, the plume can act as an along-coast conduit during downwelling when entrainment occurs. Although these events are rare and the mean latitudinal distribution remains similar, these events are critical in connecting the OR and WA coasts.

3.2.3. CR Plume Influence on Potential HAB Transport Pathways

The combined effect of the above CR-related mechanisms on potential HAB surface transport pathways from *Pn* hot spots is that the CR plume acts to mitigate the number of HAB beach events by blocking onshore transport while at the same time defining the HB transport pathway. The CR plume can block onshore transport of HABs from both source regions. In fact, total Long Beach landings are lower in the full simulations than in the No-CR simulations for both source regions. Even after entrainment into the plume, the onshore transport of particles is still reduced relative to the No-CR simulations suggesting that entrained particles are strongly influenced by the dominant alongshore momentum transport in the plume and potentially influenced by shoreward plume fronts.

While beachings on the OR coast from the northern source are limited due to the strong offshore Ekman transport that occurs during periods of upwelling winds sufficient to move particles that far south (see Figure 11b), beachings from the southern source during downwelling winds strongly depend on the CR plume. If southern source particles are entrained into the plume on a previous upwelling/relaxation cycle, they can be transported significantly farther north during downwelling winds. Entrainment is critical to formation of the Heceta Bank pathway to the WA coast. Without plume entrainment, HABs from a southern source would commonly beach along OR (see Figure 11a).

4. Discussion

Our well-validated simulations confirm the existence of both northern and southern *Pn* HAB transport pathways and elucidate the CR plume influence on potential pathways. However, the simulations predict more beaching events than seen in observed high *Pn* cell count events. In an effort to improve predictability, we further investigate wind intermittency and develop an index to capture the northern transport pathway. Additionally, we incorporate a biogeochemical model to reduce the number of false positive beaching events.

4.1. Wind Intermittency

In addition to the overall wind direction and strength, an important consideration to the seasonality and interannual variability of transport pathways is the time history of the winds. This is particularly clear in the transport from the northern source where downwelling winds are required to bring particles to the coast after upwelling winds. Figure 8 showed that during our 4 model years more particles reached the coast during the upwelling season in years with frequent relaxation/downwelling wind events (2004 and 2007). Thus, a measure of the wind intermittency may provide an additional useful predictive tool during the upwelling season (i.e., when the northern source transport pathway dominates). The most successful approach we employed was a simple algorithm that uses both the raw hourly wind stress in the major principal axes direction (τ, N m^{-2}) and an upwelling index based on the 8 day weighted mean winds in the major principal axes direction (W_{maji8d} N m^{-2}). This upwelling index is based on that defined by *Austin and Barth* [2002], although it is employed as a filter, thus retaining the units of τ:

$$W_{maj,k}(t) = \frac{1}{k}\int_0^t \tau_{maj} e^{(t'-t)/k} dt'$$

where k is the filter time (8 days in this case) and t is time. W describes the overall mean wind conditions while the wind stress, τ, represents the instantaneous winds. For transport from the northern source, the mean winds should be upwelling favorable while the instantaneous winds should be 0 or downwelling favorable (e.g., beachings in Figure 2). Thus, the wind intermittency index is a true/false index defined as:

© 2014. American Geophysical Union. All Rights Reserved.

$$I_{w8}(t)=1 \text{ if } \left(W_{maj,8d} \leq 0\right) \text{ and } \left(\tau_{maj} \geq 0\right), \text{ otherwise } I_{w8}(t)=0$$

where we have defined wind stress > 0 as downwelling favorable. The correspondence between our wind index (Figure 12a) and the presence of beachings from the Juan de Fuca Eddy (Figure 12b) is strong. The cumulative sum of this index over each upwelling season matches the patterns in the observed interannual variability; i.e., high transport potential in 2004 and 2007 and significantly lower potential in 2005 and 2006.

During the downwelling season (i.e., when the southern source transport pathway dominates), intermittency remains important as particles only reach the WA coast if entrainment in the CR plume occurs. Transport pathways to the OR coast from this southern source on the other hand are very common and only decrease when entrainment into the CR plume occurs. Entrainment of the southern source requires the plume presence (i.e., prior upwelling) and other potential factors such as a weak plume front. Unfortunately, defining an index for transport from the southern source was less successful. This is likely due to the fact that with similar wind conditions, plume entrainment sometimes occurs and sometimes does not. The time history of the wind and thus the plume location and strength, as well as the river flow are all important factors in determining whether entrainment can occur or not.

4.2. Eliminating False Positives

Most (7/9) of the *Pn* HAB events at Long Beach are captured with our particle tracking results, confirming the importance of both a northern (Juan de Fuca Eddy) and southern (Heceta Bank) source for *Pn* HAB events on the WA coast. However, as seen in Figure 8, (or using the wind index, I_w, introduced above) there are numerous false positives, i.e., on the basis of transport mechanisms alone, events may be predicted when they do not actually occur (also see Figures 12a–12c). For example, early summer 2005 (∼day 170) and mid-summer 2007 (∼day 920) events from the Juan de Fuca Eddy and intermittent winter/early spring events from the Heceta Bank region (∼days −350, 20, 360, 420, 720) are false positives. Loosely defining events as groupings of beachings where at least one particle beaches in 20 days, there are ∼24 events predicted while only 9 events are observed (∼15 false positives).

Even when a physical pathway exists, *Pn* (or other phytoplankton) may not exist in the source region. Some of the false positives occur during periods of overall low productivity; i.e., winter/early spring and early fall. For

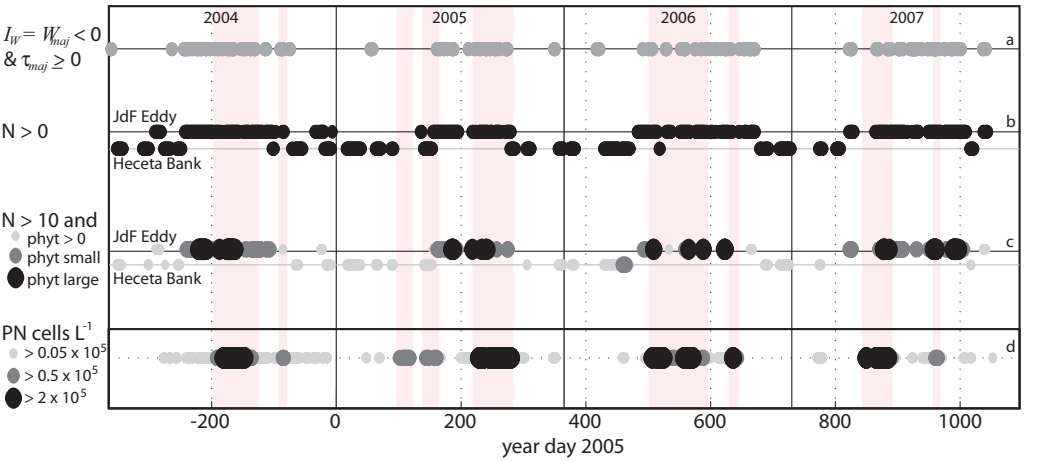

Figure 12. Particle tracking with biology. (a) Wind index representing the potential for beach landings originating from the Juan de Fuca Eddy as described in section 4. (b) Particle hits at Long Beach, a dot indicates one or more hits from either the northern source (upper line) or southern source (lower line). (c) Thresholding approach incorporating the biogeochemical model. All dots have 10 or more particles reaching the beach while size/color represents the mean cumulative sum of along-path phytoplankton in the model (phytoplankton values greater than background levels are in small light gray dots while large phytoplankton values are in large black dots, larger than 125 μg L^{-1}). (d) Observed *Pn* cell count (cells L^{-1}) at Long Beach from the ORHAB program split into three bins ranging from a small number of cells (small light gray dots) to a large number of cells (large black dots). Pink rectangles outline the observed events as also marked in Figure 8.

© 2014. American Geophysical Union. All Rights Reserved.

example, the Eddy is most productive in summer through late fall [*Trainer et al*., 2009]. While extensive in situ biological measurements have not found a clear correlation between *Pn* and nutrients or water properties in the PNW, they have found a significant, positive correlation between *Pn* and total chlorophyll [*Trainer et al*., 2009]. Thus, periods with low overall productivity, such as winter/early spring and early summer, may have physical transport pathways from the source regions to the coast but the water may not contain *Pn* cells.

As a first cut to identifying false positives, we include results from a biogeochemical model in our particle tracking analysis. The biological model [described in *Banas et al*., 2009a; Davis et al., manuscript in preparation, 2014] contains nutrients, one phytoplankton class, one microzooplankton class, small and large detritus, and oxygen. Biogeochemical parameters (such as growth rate, grazing rate, etc.) were chosen based on extensive in situ measurements. The biogeochemical model is coupled to the hydrodynamic simulations and results compare well with observed chlorophyll, primary productivity, and nitrate.
As a simple test to utilize this model to eliminate false positives, we employ a thresholding approach. Figure 12c includes an example thresholding with cutoffs requiring more than 10 particles reaching the beach and varying levels of the mean cumulative sum of the along-path phytoplankton values. This approach reduces the number of false positives significantly (by more than 80%), predicting only two false positives. Seven out of the nine observed events are predicted while two are considered missed events. It does not remove false-positives entirely as the onset and length of events differ, thus additional predictive skill on event scales is desired.

To improve predictability, further research on *Pn* growth in the PNW is required to determine what conditions are preferential for *Pn* cell growth and subsequently for toxin production. Current research by Lubetkin and Lessard (manuscript in preparation, 2014) employs nonparametric multiplicative regression models to try to determine what drives development of *Pn* and DA in the PNW. The results from this analysis will be combined with our modeling approach in the future to improve *Pn* HAB prediction capabilities. To capture the early spring blooms from Heceta Bank including the small coastal estuaries may improve predictability. These events occur prior to the spring transition when the upwelling-driven nutrient supply is low. *Wetz et al*. [2006] showed that local winter riverine inputs of nutrients along the OR coast could initiate late winter/early spring blooms consistent with this potential source. Finally, an additional, promising way to improve predictability is a combined monitoring/modeling approach as has been recently suggested [e.g., *Jochens et al*., 2010]. In the PNW, shipboard monitoring for *Pn* and DA within the generation hot spots will allow for particle tracking models like this one to be run in a predictive mode to assess the risk that an observed bloom will reach the shore.

5. Conclusions

Here we have described a realistic numerical model for the PNW coastal region. This manuscript presents detailed validation of the model physics using extensive observations. We show that the model adequately simulates currents and water properties along the coast throughout depth over the shelf and shelf break. For example, important coastal processes such as river plumes, CTWs, coastal upwelling, and CUC dynamics, amongst other processes are consistent with observational data in both spatial patterns and dominant temporal variability.

This manuscript uses this model to investigate potential HAB transport pathways in the PNW. In particular, we investigate transport pathways from previously identified *Pn*/DA source regions to the WA coast. Overall, we observe a strong seasonal signal in transport pathways associated with the change in the direction of the predominant seasonal regional currents and local upwelling/downwelling favorable winds. During the summer/fall upwelling season, beach events are most often associated with transport from the northern source, the Juan de Fuca Eddy. While during the winter/early spring downwelling season, the model is consistent with the hypothesis that the southern source, Heceta Bank, can be a source to the WA coast. The CR plume mitigates beachings by blocking onshore transport. The CR influence in the alongshore direction is variable, but important for allowing the southern source pathway to the WA coast via plume entrainment. Understanding the mechanisms for entrainment into regional river plumes as well as transport within the nearshore zone are important research areas that would further improve understanding potential HAB transport pathways in the PNW.

The transport simulations and a wind intermittency index capture *Pn* HAB beach events, yet result in numerous false positives. Predictability is enhanced by $>$80% with the incorporation of a simple biogeochemical model. Nevertheless, additional research on the biological drivers of *Pn* growth and DA production in the

© 2014. American Geophysical Union. All Rights Reserved.

Table A1. Model Skill Comparison[a]

	NCOM	MoSSea	Coastal Cascadia			
			Low	High	Medium	
Δx (km)	14	0.3 - 6	3	1 - 3	1.5 - 4	1.5 - 4
N	40	20	20	40	40	40
U	-0.09	-0.35	-0.31	-0.39	-0.11	-0.11
V	0.06	-0.27	-0.27	-0.30	-0.15	-0.18
S	-12.83	-2.16	-16.45	-1.47	-1.25	-0.91
T	-0.30	0.23	-1.00	0.15	-0.05	-0.30
S (casts)	0.07	0.85	0.64	0.77	0.77	0.75
T (casts)	0.61	0.88	0.63	0.85	0.85	0.86
η	0.01	0.93	0.92	0.92	0.89	0.89
$<U>$	-1.19	-0.46	-0.22	-0.46	-0.08	-0.31
$<V>$	-0.89	-0.13	-0.03	-0.10	0.06	0.06
$<S>$	-13.11	-2.13	-16.55	-1.44	-1.16	-0.89
$<T>$	-1.01	0.27	-1.11	0.07	-0.13	-0.48
$<\eta>$	0.68	0.70	0.59	0.62	0.72	0.68
average	**-2.33**	**-0.14**	**-2.76**	**-0.06**	**0.03**	**0.01**

[a]Comparison of model skill score (*SS*) for various simulations for the year 2005. NCOM is the NCOM global model, MoSSea is the model published in *Sutherland et al.* [2011], and Low, Medium, and High indicate the lowest, medium, and highest Cascadia coastal model resolutions, respectively. Variables with brackets, $< >$, indicate subtidal data, while those without brackets are hourly data. *U* and *V* are east/west and north/south velocities, respectively. Several different boundary conditions for the final medium resolution model were compared as described in the text. Here only two medium resolution runs are included; both have the final parameters (ROMS options ADD_FSOBC and ADD_M2OBC are activated, $T_{in} = 0.75$ days and $T_{out} = 360$ days). Note that the other ROMS columns do not have these options and have $T_{in} = 0.75$ days, $T_{out} = 3$ days. The two medium resolution runs presented differ only in the initial conditions: the first was initialized using NCOM, the second using ROMS output from the end of the previous year. Differences in skill between these two runs are indicative of the inherent variability in model skill score between runs. Colors are coded such that the darkest gray on any row is the least skillful model run, and white is the most skillful.

PNW is required to enhance predictability. A combined in situ monitoring/modeling approach would also significantly aid HAB predictability in the PNW.

Appendix A: Additional Model Information and Validation

A1. Numerical Simulations

The model described in section 2.1 utilizes realistic bathymetry, forcing and initial conditions. High-resolution bathymetry [*Smith and Sandwell*, 1997; *Haugerud*, 2000; *Finlayson*, 2005] was smoothed using a volume-preserving scheme to decrease numerical errors near steep slopes while best preserving the original bathymetry [*Sikiric*, 2011]. The model is initialized and nudged at the western and southern boundaries with the global Navy Coastal Ocean Model (NCOM) [*Barron et al*., 2006, 2007]. Radiation conditions are used on all 3-D model fields at the open boundaries [*Marchesiello et al*., 2001, 2003] and open boundary conditions for free-surface and depth-averaged momentum use the *Chapman* [1985] and *Flather* [1976] conditions, respectively. The northern boundary is closed at Johnstone Strait. In reality, exchange through this narrow strait can be significant; however, tests employing an open northern boundary forced with tides from *Foreman et al*. [2012] did not significantly improve model skill. In addition, we tested different implementations of the open boundary conditions (described in section A2). The model includes 16 river point sources using daily discharge values from the United States Geological Survey (USGS, http://waterdata.usgs.gov/usa/nwis/) and Environment Canada (http://www.wsc.ec.gc.ca/applications/H2O/). These include 14 Puget Sound rivers, the Fraser River, and the Columbia River (note that the smaller coastal rivers are not included). Eight tidal constituents derived from the 1/4° TPXO7.2 inverse global tidal model [*Egbert and Erofeeva*, 2002] are forced at the open boundaries. Meteorological forcing of surface pressure, wind, air temperature, relative humidity, shortwave radiation, downward longwave radiation, and rainfall are taken from the MM5 regional forecast model [*Mass et al*., 2003].

A2. Model Validation—Overall Model Skill

The model currents, salinity, and temperature are validated using an extensive array of observations described in section 2.3.1 (see Figure 1). We utilized three different model skill metrics to assess the simulation performance and test different model setups: the Skill Score (*SS*) [*Murphy*, 1988], Willmott Skill Score (*WS*) [*Willmott*, 1982], and correlation coefficient (*r*), discussed in more depth in *Liu et al*. [2009b] and *Sutherland et al*. [2011]. The skill scores are defined as:

$$SS = 1 - \frac{\frac{1}{N}\sum_{i=1}^{i=N}(m_i - o_i)^2}{\frac{1}{N}\sum_{i=1}^{i=N}(o_i - \overline{o})^2} = 1 - \frac{MSE}{s_o^2}$$

© 2014. American Geophysical Union. All Rights Reserved.

$$WS = 1 - \frac{\frac{1}{N}\sum_{i=1}^{i=N}(m_i - o_i)^2}{\frac{1}{N}\sum_{i=1}^{i=N}(|m_i - \overline{o}| + |o_i - \overline{o}|)^2} = 1 - \frac{MSE}{\frac{1}{N}\sum_{i=1}^{i=N}(|m_i - \overline{o}| + |o_i - \overline{o}|)^2}$$

$$r = \frac{\frac{1}{N-1}\sum_{i=1}^{i=N}(m_i - \overline{m})(o_i - \overline{o})}{\frac{1}{N-1}\sqrt{\sum_{i=1}^{i=N}(m_i - \overline{m})^2}\sqrt{\sum_{i=1}^{i=N}(o_i - \overline{o})^2}} = \frac{s_{mo}}{s_m s_o}$$

where m_i is a model value, o_i is an observational value, and there are N paired modeled/observed values. *MSE* is the mean square error, s_{xy} is the covariance of x and y, s_x is the standard deviation of x, and s_x^2 is the variance of x. The *SS* is a valuable metric to compare models to one another where a higher *SS* indicates better model performance [*Murphy*, 1988], thus we use the *SS* to compare our different model setups and boundary conditions. The *WS* is an index of agreement between modeled and observed values where a *WS* of 1 indicates complete agreement and a *WS* of 0 indicates complete disagreement [*Willmott*, 1982]. Here we use the *WS* to compare our chosen model with observations.

We compared our various resolution models (along with the higher Salish Sea resolution model, MoSSea) and determined that while our lowest resolution grid clearly had the least skill (performing similarly poorly to NCOM global), the medium resolution grid had sufficient skill compared to our highest resolution grid and the MoSSea grid (see Appendix Table A1 where darker colors indicate worse performance). We further tested the medium resolution grid with different open boundary conditions (including nudging time scales, a sponge layer, and the implementation of tides) and different vertical resolution. In summary, our final model runs use the medium resolution grid and include an outgoing nudging time scale of 360 days [as in *Marchesiello et al.*, 2001], no sponge layer, activated ADD_FSOBC and ADD_M2OBC options, and 40 vertical layers (see the last two columns of Appendix Table A1).

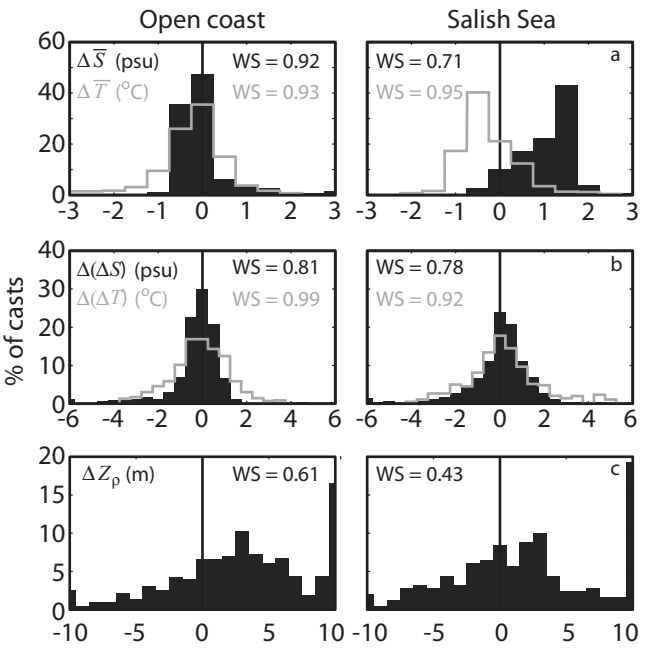

Figure A1. CTD cast histograms. (a) Histograms (% of total CTD casts) of the difference in the depth mean salinity (solid black) and temperature (gray line) between the model and observations. Values less than zero indicate the model is fresher or colder. (b) Histograms of the difference in the vertical stratification between the model and observations. Vertical stratification is measured as the difference between the top and bottom layer salinities (solid black) and temperatures (gray line). Values less than zero indicate the model is less stratified than the observations. (c) Histograms of the difference in the pycnocline depths between the model and observations. Values greater than zero indicate the model has a shallower pycnocline depth. Several values fall into the far right bin indicating that the algorithm (which searches for the maximum density gradient) found a particularly deep pycnocline in the observations. Some casts contain noisy data or steps that can lead to the selection of an erroneously deep pycnocline value. All three measures are split into two regional groups, (left) the open coast region and (right) the Salish Sea. *WS*s for all comparisons are included in each panel.

*WS*s for the final simulations during 2005 are shown in Table 1. The *WS* is computed for all time series from all available moorings during the observational period at all available depths.

For most of the moorings (ECOHAB-EH and RISE-R), observations exist during the summer in 2–4 m intervals throughout most of the depth for velocity and at a few fixed points in the vertical for salinity and temperature. For example, EH2 (comparison presented in Figure 3) includes velocity between ~12 and 40 m every 2 m, temperature at 1, 4, 10, 11, 15, 20, 29, 39, and 49 m, and salinity at 4, 15, and 39 m from 1 May 2005 to 3 October 2005. The A1 and J2C moorings (maintained by IOS) and Race Rocks (RR, near-surface measurements maintained by the Race Rocks Ecological Reserve/Marine Protected Area and available via

© 2014. American Geophysical Union. All Rights Reserved.

IOS) are nearly year-round time series. *WS*s are computed on the minor and major velocity components defined by principal axes analysis as well as on the hourly and subtidal time series. Average *WS*s are strong (Table 1, 1 indicates perfect agreement, 0 complete disagreement), particularly for the major principal axes velocity component and temperature. Salinity agreement is weaker because of a salinity bias that is inherited from the NCOM boundary conditions [*Liu et al*., 2009b; *Sutherland et al*., 2011]. *WS*s are lowest (worst) beyond the shelf break (A1 and EH3) and highest (best) on the shelf (EH2, EH4, RN, RC, and RS).

Overall, *WS* for the salinity and temperature from all of the 2264 CTD casts in 2005 (see Figure 1) are high ($\geq$0.92, Table 1a, far right-hand column). These values aggregate important features of the salinity and temperature vertical structure. Thus, we also made comparisons similar to *Sutherland et al*. [2011] which examine histograms of the depth mean salinity and temperature, stratification defined by two layers (when possible, top-bottom difference when there is no distinct pycnocline), and the depth of the pycnocline (when it exists) in two regions, along the open coast and within the Salish Sea (Appendix Figure A1). The model is too salty and cold within the Salish Sea (by $\sim$1.5 psu and $\sim$0.5°C), but does well along the coast. The two-layer stratification compares well in both regions. Finally, the model depth of stratification tends to be slightly shallower than the observations because individual model profiles are typically smoother than observations.

Finally, Table 1b shows the *WS* for the sea surface elevation at 12 NOAA tide gauges (adjusted with atmospheric pressure from NDBC buoys, www.ndbc.noaa.gov/, see Figure 1) moving from south to north and into the Salish Sea. Tidal sea surface elevations compare strongly throughout the domain, weakening slightly within the Salish Sea (*WS* $\geq$ 0.93). Subtidal sea surface elevation has slightly lower *WS* than the tidal values.

Acknowledgments

Special thanks to S. Geier (multiyear moored sensors) and N. Kachel (CTD data) from the ECOHAB-PNW and RISE projects, E. Dever (multiyear moored sensors from the RISE project), R. Thomson (moored arrays and CTD data, Fisheries and Oceans Canada Institute of Ocean Sciences, IOS), A. Odell (*Pn* cell count data, Olympic Regional Harmful Algal Blooms Partnership, ORHAB), B. Peterson (multiyear OR CTD data), the National Oceanic and Atmospheric Administration (NOAA, CTD data, and tide gauges), the Olympic Coast National Marine Sanctuary (OCNMS, multiyear WA moored sensors), the Puget Sound Regional Synthesis Model (PRISM, Puget Sound CTD data), Washington State Department of Ecology (DOE, Puget Sound CTD data), King County Puget Sound Marine Monitoring (Puget Sound CTD data), and the Hood Canal citizen monitoring project (Hood Canal CTD data) for use of their data. Thanks to other members of the PNWTOX and UWCMG groups for useful discussions including M. Foreman, R. Thomson, I. Fine, E. Lessard, S. Lubetkin, R. McCabe, D. Sutherland, and K. Thyng. D. Darr provided computer cluster administration and support. In addition, this work was facilitated through the use of advanced computational, storage, and networking infrastructure provided by the Hyak supercomputer system, supported in part by the University of Washington eScience Institute. Model run setup files and output used in this manuscript are available upon request. This work was supported by grants from the Coastal Ocean Program of the National Oceanic and Atmospheric Administration (NOAA) (NA09NOS4780180) and the National Science Foundation (NSF) (OCE0942675) as part of the Pacific Northwest Toxins (PNWTOX) project. The statements, findings, conclusions, and recommendations are those of the participants/authors and do not reflect the views of NSF, NOAA, or the Department of Commerce. This work was supported by grants. This is ECOHAB and PNWTOX Contributions #792 and #11.

References

Adams, N., A. MacFadyen, B. Hickey, and V. Trainer (2006), The nearshore advection of a toxigenic *Pseudo-nitzschia* bloom and subsequent domoic acid contamination of intertidal bivalves, *Afr. J. Mar. Sci.*, *28*(2), 271–276, doi:10.2989/18142320609504161.

Anderson, D. M., A. D. Cembella, and G. M. Hallegraeff (2012), Progress in understanding harmful algal blooms: Paradigm shifts and new technologies for research, monitoring, and management, *Annu. Rev. Mar. Sci.*, *4*(1), 143–176, doi:10.1146/annurev-marine-120308-081121.

Austin, J. A., and J. A. Barth (2002), Variation in the position of the upwelling front on the Oregon shelf, *J. Geophys. Res.*, *107*, 3180, doi:10.1029/2001JC000858.

Austin, J. A., and S. J. Lentz (2002), The inner shelf response to wind-driven upwelling and downwelling, *J. Phys. Oceanogr.*, *32*(7), 2171–2193, doi:10.1175/1520-0485(2002)032<2171:TISRTW>2.0.CO;2.

Banas, N. S., P. MacCready, and B. M. Hickey (2009a), The Columbia River plume as cross-shelf exporter and along-coast barrier, *Cont. Shelf Res.*, *29*(1), 292–301, doi:10.1016/j.csr.2008.03.011.

Banas, N., P. McDonald, and D. Armstrong (2009b), Green crab larval retention in Willapa Bay, Washington: An intensive Lagrangian modeling approach, *Estuaries Coasts*, *32*(5), 893–905, doi:10.1007/s12237-009-9175-7.

Barron, C. N., A. B. Kara, P. J. Martin, R. C. Rhodes, and L. F. Smedstad (2006), Formulation, implementation and examination of vertical coordinate choices in the Global Navy Coastal Ocean Model (NCOM), *Ocean Modell.*, *11*(3), 347–375.

Barron, C. N., L. F. Smedstad, J. M. Dastugue, and O. M. Smedstad (2007), Evaluation of ocean models using observed and simulated drifter trajectories: Impact of sea surface height on synthetic profiles for data assimilation, *J. Geophys. Res.*, *112*, C07019, doi:10.1029/2006JC003982.

Battisti, D. S., and B. M. Hickey (1984), Application of remote wind-forced coastal trapped wave theory to the Oregon and Washington coasts, *J. Phys. Oceanogr.*, *14*, 887–935.

Beckers, J. M., and M. Rixen (2003), EOF calculations and data filling from incomplete oceanographic datasets, *J. Atmos. Oceanic Technol.*, *20*(12), 1839–1856, doi:10.1175/1520-0426(2003)020<1839:ECADFF>2.0.CO;2.

Bejarano, A. C., F. M. VanDola, F. M. Gulland, T. K. Rowles, and L. H. Schwacke (2008), Production and toxicity of the marine biotoxin domoic acid and its effects on wildlife: A review, *Hum. Ecol. Risk Assess.*, *14*(3), 544–567, doi:10.1080/10807030802074220.

Burla, M., A. M. Baptista, Y. Zhang, and S. Frolov (2010), Seasonal and interannual variability of the Columbia River plume: A perspective enabled by multiyear simulation databases, *J. Geophys. Res.*, *115*, C00B16, doi:10.1029/2008JC004964.

Castelao, R. M., and J. A. Barth (2006), The relative importance of wind strength and along-Shelf bathymetric variations on the separation of a coastal upwelling jet, *J. Phys. Oceanogr.*, *36*(3), 412–425, doi:10.1175/JPO2867.1.

Chapman, D. C. (1985), Numerical treatment of cross-shelf open boundaries in a barotropic coastal ocean model, *J. Phys. Oceanogr.*, *15*(8), 1060–1075, doi:10.1175/1520-0485(1985)015<1060:NTOCSO>2.0.CO;2.

Connolly, T. P., and B. M. Hickey (2014), Regional impact of submarine canyons during seasonal upwelling, *J. Geophys. Res.*, *119*, 953–975, doi:10.1002/2013JC009452.

Connolly, T. P., B. M. Hickey, I. Shulman, and R. E. Thomson (2014), Coastal trapped waves, alongshore pressure gradients, and the California Undercurrent, *J. Phys. Oceanogr.*, *1*, 319–342, doi:10.1175/JPO-D-13-095.1.

Denman, K. L., and H. J. Freeland (1985), Correlation scales, objective mapping and a statistical test of geostrophy over the continental shelf, *J. Mar. Res.*, *43*(3), 517–539, doi:10.1357/002224085788440402.

Dyson, K., and D. D. Huppert (2010), Regional economic impacts of razor clam beach closures due to harmful algal blooms (HABs) on the Pacific coast of Washington, *Harmful Algae*, *9*(3), 264–271, doi:10.1016/j.hal.2009.11.003.

Egbert, G. D., and S. Y. Erofeeva (2002), Efficient inverse modeling of barotropic ocean tides, *J. Atmos. Oceanic Technol.*, *19*(2), 183–204, doi:10.1175/1520-0426(2002)019<0183:EIMOBO>2.0.CO;2.

Emery, W. J., and R. E. Thomson (2004), *Data Analysis Methods in Physical Oceanography*, 2nd ed., 638 pp., Elsevier, Amsterdam.

Finlayson, D. P. (2005), *Combined Bathymetry and Topography of the Puget Sound Lowland*, Univ. of Washington, Seattle, Wash. [Available at http://www.ocean.washington.edu/data/pugetsound/.].

© 2014. American Geophysical Union. All Rights Reserved.

Flament, P. (2002), A state variable for characterizing water masses and their diffusive stability: Spiciness, *Prog. Oceanogr.*, *54*(1–4), 493–501, doi:10.1016/S0079-6611(02)00065-4.
Flather, R. A. (1976), A tidal model of the northwest European continental shelf, *Mem. Soc. R. Sci. Liege, Ser.*, *10*(6), 141–164.
Fong, D. A., and W. R. Geyer (2002), The alongshore transport of freshwater in a surface-trapped river plume, *J. Phys. Oceanogr.*, *32*(3), 957–972, doi:10.1175/1520-0485(2002)032<0957:TATOFI>2.0.CO;2.
Foreman, M. G. G., W. Callendar, A. MacFadyen, B. M. Hickey, R. E. Thomson, and E. Di Lorenzo (2008), Modeling the generation of the Juan de Fuca Eddy, *J. Geophys. Res.*, *113*, C03006, doi:10.1029/2006JC004082.
Foreman, M. G. G., D. J. Stucchi, K. A. Garver, D. Tuele, J. Isaac, T. Grime, M. Guo, and J. Morrison (2012), A circulation model for the Discovery Islands, British Columbia, *Atmos. Ocean*, *50*(3), 301–316, doi:10.1080/07055900.2012.686900.
Franks, P. J. S. (1997), Models of harmful algal blooms, *Limnol. Oceanogr.*, *42*, 1273–1782.
Haugerud, R. A. (2000), Digital elevation model (DEM) of Cascadia, latitude 39N–53N, longitude 116W–133W, *U.S. Geol. Surv. Open File Rep., 99–369*, Menlo Park. [Available at http://geopubs.wr.usgs.gov/open-file/of99-369.].
Hickey, B., S. Geier, N. Kachel, and A. MacFadyen (2005), A bi-directional river plume: The Columbia in summer, *Cont. Shelf Res.*, *25*(14), 1631–1656, doi:10.1016/j.csr.2005.04.010.
Hickey, B., R. McCabe, S. Geier, E. Dever, and N. Kachel (2009), Three interacting freshwater plumes in the northern California Current System, *J. Geophys. Res.*, *114*, C00B03, doi:10.1029/2008JC004907.
Hickey, B. M. (1979), The California current system—Hypotheses and facts, *Prog. Oceanogr.*, *8*(4), 191–279, doi:10.1016/0079-6611(79)90002-8.
Hickey, B. M. (1989), Patterns and processes of shelf and slope circulation, in *Coastal Oceanography of Washington and Oregon*, edited by M. R. Landry and B. M. Hickey, pp. 41–115, Elsevier Sci., Amsterdam.
Hickey, B. M. (1998), Coastal oceanography of western North America from the tip of Baja California to Vancouver Island: Coastal segment, in *The Sea*, vol. 11, edited by A. R. Robinson and K. H. Brink, pp. 345–391, John Wiley, Hoboken, N. J.
Hickey, B. M., and N. S. Banas (2003), Oceanography of the US Pacific Northwest Coastal Ocean and estuaries with application to coastal ecology, *Estuaries*, *26*(4), 1010–1031, doi:10.1007/BF02803360.
Hickey B. M., and N. S. Banas (2008), Why is the northern end of the California Current System so productive?, *Oceanography*, *21*, 90–107, doi:10.5670/oceanog.2008.07.
Hickey, B. M., R. E. Thomson, H. Yih, and P. H. LeBlond (1991), Velocity and temperature fluctuations in a buoyancy-driven current off Vancouver Island, *J. Geophys. Res.*, *96*, 10,507–10,538, doi:10.1029/90JC02578.
Hickey, B. M., et al. (2010), River influences on shelf ecosystems: Introduction and synthesis, *J. Geophys. Res.*, *115*, C00B17, doi:10.1029/2009JC005452.
Hickey, B. M., V. L. Trainer, P. Michael Kosro, N. G. Adams, T. P. Connolly, N. B. Kachel, and S. L. Geier (2013), A springtime source of toxic *Pseudo-nitzschia* cells on razor clam beaches in the Pacific Northwest, *Harmful Algae*, *25*, 1–14, doi:10.1016/j.hal.2013.01.006.
Holt, C. A., and N. Mantua (2009), Defining spring transition: regional indices for the California Current System, *Mar. Ecol. Prog. Ser.*, *393*, 285–299, doi:10.3354/meps08147.
Huyer, A., E. J. C. Sobey, and R. L. Smith (1979), The spring transition in currents over the Oregon Continental Shelf, *J. Geophys. Res.*, *84*(C11), 6995–7011, doi:10.1029/JC084iC11p06995.
Jochens, A. E., T. C. Malone, R. P. Stumpf, B. M. Hickey, M. Carter, R. Morrison, J. Dyble, B. Jones, and V. L. Trainer (2010), Integrated ocean observing system in support of forecasting harmful algal blooms, *Mar. Technol. Soc. J.*, *44*(6), 99–121, doi:10.4031/MTSJ.44.6.16.
Kim, S., and J. A. Barth (2011), Connectivity and larval dispersal along the Oregon coast estimated by numerical simulations, *J. Geophys. Res.*, *116*, C06002, doi:10.1029/2010JC006741.
Kirincich, A. R., and J. A. Barth (2009), Alongshelf variability of inner-shelf circulation along the Central Oregon Coast during summer, *J. Phys. Oceanogr.*, *39*(6), 1380–1398, doi:10.1175/2008JPO3760.1.
Kosro, P. M. (2005), On the spatial structure of coastal circulation off Newport, Oregon, during spring and summer 2001 in a region of varying shelf width, *J. Geophys. Res.*, *110*, C10S06, doi:10.1029/2004JC002769.
Kosro, P. M., W. T. Peterson, B. M. Hickey, R. K. Shearman, and S. D. Pierce (2006), Physical versus biological spring transition: 2005, *Geophys. Res. Lett.*, *33*, L22S03, doi:10.1029/2006GL027072.
Kudela, R. M., S. Seeyave, and W. P. Cochlan (2010), The role of nutrients in regulation and promotion of harmful algal blooms in upwelling systems, *Prog. Oceanogr.*, *85*(1–2), 122–135, doi:10.1016/j.pocean.2010.02.008.
Lentz, S. J., and M. R. Fewings (2012), The wind- and wave-driven inner-shelf circulation, *Annu. Rev. Mar. Sci.*, *4*(1), 317–343, doi:10.1146/annurev-marine-120709-142745.
Liu, Y., P. MacCready, and B. M. Hickey (2009a), Columbia River plume patterns in summer 2004 as revealed by a hindcast coastal ocean circulation model, *Geophys. Res. Lett.*, *36*, L02601, doi:10.1029/2008GL036447.
Liu, Y., P. MacCready, B. M. Hickey, E. P. Dever, P. M. Kosro, and N. S. Banas (2009b), Evaluation of a coastal ocean circulation model for the Columbia River plume in summer 2004, *J. Geophys. Res.*, *114*(C2), C00B04, doi:10.1029/2008JC004929.
Lynn, R. J., S. J. Bograd, T. K. Chereskin, and A. Huyer (2003), Seasonal renewal of the California Current: The spring transition off California, *J. Geophys. Res.*, *108*(C8), 3279, doi:10.1029/2003JC001787.
MacCready, P., N. S. Banas, B. M. Hickey, E. P. Dever, and Y. Liu (2009), A model study of tide- and wind-induced mixing in the Columbia River Estuary and plume, *Cont. Shelf Res.*, *29*(1), 278–291, doi:10.1016/j.csr.2008.03.015.
MacFadyen, A., and B. M. Hickey (2010), Generation and evolution of a topographically linked, mesoscale eddy under steady and variable wind-forcing, *Cont. Shelf Res.*, *30*(13), 1387–1402, doi:10.1016/j.csr.2010.04.001.
MacFadyen, A., B. M. Hickey, and M. G. G. Foreman (2005), Transport of surface waters from the Juan de Fuca eddy region to the Washington coast, *Cont. Shelf Res.*, *25*(16), 2008–2021, doi:10.1016/j.csr.2005.07.005.
MacFadyen, A., B. M. Hickey, and W. P. Cochlan (2008), Influences of the Juan de Fuca Eddy on circulation, nutrients, and phytoplankton production in the northern California Current System, *J. Geophys. Res.*, *113*, C08008, doi:10.1029/2007JC004412.
Marchesiello, P., J. C. McWilliams, and A. Shchepetkin (2001), Open boundary conditions for long-term integration of regional oceanic models, *Ocean Modell.*, *3*(1–2), 1–20, doi:10.1016/S1463-5003(00)00013-5.
Marchesiello, P., J. C. McWilliams, and A. Shchepetkin (2003), Equilibrium structure and dynamics of the California Current System, *J. Phys. Oceanogr.*, *33*, 753–783, doi:10.1175/1520-0485(2003)33<753:ESADOT>2.0.CO;2.
Marchetti, A., V. L. Trainer, and P. J. Harrison (2004), Environmental conditions and phytoplankton dynamics associated with *Pseudo-nitzschia* abundance and domoic acid in the Juan de Fuca eddy, *Mar. Ecol. Prog. Ser.*, *281*, 1–12, doi:10.3354/meps281001.
Mass, C. F., et al. (2003), Regional environmental prediction over the Pacific Northwest, *Bull. Am. Meteorol. Soc.*, *84*(10), 1353–1366, doi:10.1175/BAMS-84-10-1353.

© 2014. American Geophysical Union. All Rights Reserved.

Murphy, A. H. (1988), Skill scores based on the mean square error and their relationships to the correlation coefficient, *Mon. Weather Rev.*, *116*(12), 2417–2424, doi:10.1175/1520-0493(1988)116<2417:SSBOTM>2.0.CO;2.
North, E. W., Z. Schlag, R. R. Hood, M. Li, L. Zhong, T. Gross, and V. S. Kennedy (2008), Vertical swimming behavior influences the dispersal of simulated oyster larvae in a coupled particle-tracking and hydrodynamic model of Chesapeake Bay, *Mar. Ecol. Prog. Ser.*, *359*, 99–115, doi:10.3354/meps07317.
Pelland, N. A., C. C. Eriksen, and C. M. Lee (2013), Subthermocline eddies over the Washington continental slope as observed by Seagliders, 2003–09, *J. Phys. Oceanogr.*, *43*, 2025–2053, doi:10.1175/JPO-D-12-086.1.
Pierce, S. D., R. L. Smith, P. M. Kosro, J. A. Barth, and C. D. Wilson (2000), Continuity of the poleward undercurrent along the eastern boundary of the mid-latitude north Pacific, *Deep Sea Res., Part II*, *47*(5–6), 811–829, doi:10.1016/S0967-0645(99)00128-9.
Pitcher, G. C., F. G. Figueiras, B. M. Hickey, and M. T. Moita (2010), The physical oceanography of upwelling systems and the development of harmful algal blooms, *Prog. Oceanogr.*, *85*, 5–32, doi:10.1016/j.pocean.2010.02.002.
Rao, S., J. Pringle, and J. Austin (2011), Upwelling relaxation and estuarine plumes, *J. Geophys. Res.*, *116*, C09023, doi:10.1029/2010JC006739.
Rivas, D., and R. M. Samelson (2011), A numerical modeling study of the upwelling source waters along the Oregon Coast during 2005, *J. Phys. Oceanogr.*, *41*(1), 88–112, doi:10.1175/2010JPO4327.1.
Schnetzer, A., P. E. Miller, R. A. Schaffner, B. A. Stauffer, B. H. Jones, S. B. Weisberg, P. M. DiGiacomo, W. M. Berelson, and D. A. Caron (2007), Blooms of *Pseudo-nitzschia* and domoic acid in the San Pedro Channel and Los Angeles harbor areas of the Southern California Bight, 2003–2004, *Harmful Algae*, *6*(3), 372–387, doi:10.1016/j.hal.2006.11.004.
Shchepetkin, A. F., and J. C. McWilliams (2005), The regional oceanic modeling system (ROMS): A split-explicit, free-surface, topography-following-coordinate oceanic model, *Ocean Modell.*, *9*(4), 347–404, doi:10.1016/j.ocemod.2004.08.002.
Sikiric, M. D. (2011), *Manual of the MATLAB Scripts of LP Bathymetry*. [Available at http://drobilica.irb.hr/~mathieu/Bathymetry/.]
Smith, W. H. F., and D. T. Sandwell (1997), Global sea floor topography from satellite altimetry and ship depth soundings, *Science*, *277*(5334), 1956–1962.
Sutherland, D. A., P. MacCready, N. S. Banas, and L. F. Smedstad (2011), A model study of the Salish Sea estuarine circulation, *J. Phys. Oceanogr.*, *41*(6), 1125–1143, doi:10.1175/2011JPO4540.1.
Thomson, R. E., and M. V. Krassovski (2010), Poleward reach of the California Undercurrent extension, *J. Geophys. Res.*, *115*, C09027, doi:10.1029/2010JC006280.
Thomson, R. E., B. M. Hickey, and P. H. LeBlond (1989), The Vancouver Island coastal current: Fisheries barrier and conduit, in *Effects of Ocean Variability on Recruitment and an Evaluation of Parameters used in Stock Assessment Models, Can. Spec. Publ. Fish. Aquat. Sci.* 108: 379 p. edited by Richard J. Beamish and G. McFarlane, pp. 265–296, Spec. Publ. of Fish. and Aquat. Sci, Ottawa, Canada.
Thomson, R. E., S. F. Mihály, and E. A. Kulikov (2007), Estuarine versus transient flow regimes in Juan de Fuca Strait, *J. Geophys. Res.*, *112*, C09022, doi:10.1029/2006JC003925.
Trainer, V. L., and M. Suddleson (2005), Monitoring approaches for early warning of domoic acid events in Washington State, *Oceanography*, *18*(2), 228–237, doi:10.5670/oceanog.2005.56.
Trainer, V. L., N. G. Adams, B. D. Bill, C. M. Stehr, J. C. Wekell, P. Moeller, M. Busman, and D. Woodruff (2000), Domoic acid production near California coastal upwelling zones, June 1998, *Limnol. Oceanogr.*, *45*, 1818–1833.
Trainer, V. L., N. G. Adams, and J. C. Wekell (2001), Domoic acid-producing Pseudo-nitzschia species off the US west coast associated with toxification events, in *Proceedings of the Ninth International Conference on Harmful Algal Blooms*, edited by G. M. Hallegraeff S. I. Blackburn C. J. Bolch, and R. J. Lewis, UNESCO, Paris, France.
Trainer, V. L., B. M. Hickey, and R. A. Horner (2002), Biological and physical dynamics of domoic acid production off the Washington coast, *Limnol. Oceanogr.*, *47*, 1438–1446.
Trainer, V. L., B. M. Hickey, E. J. Lessard, W. P. Cochlan, C. G. Trick, M. L. Wells, A. MacFadyen, and S. K. Moore (2009), Variability of *Pseudo-nitzschia* and domoic acid in the Juan de Fuca eddy region and its adjacent shelves, *Limnol. Oceanogr.*, *54*(1), 289–308, doi:10.1029/2006JC003925.
Trainer, V. L., G. C. Pitcher, B. Reguera, and T. J. Smayda (2010), The distribution and impacts of harmful algal bloom species in eastern boundary upwelling systems, *Prog. Oceanogr.*, *85*, 33–52, doi:10.1016/j.pocean.2010.02.003.
Trainer, V. L., S. S. Bates, N. Lundholm, A. E. Thessen, W. P. Cochlan, N. G. Adams, and C. G. Trick (2012), *Pseudo-nitzschia* physiological ecology, phylogeny, toxicity, monitoring and impacts on ecosystem health, *Harmful Algae*, *14*, 271–300, doi:10.1016/j.hal.2011.10.025.
Tully, J. P. (1941), Surface non-tidal currents in the approaches to Juan de Fuca strait, *J. Fish. Res. Board Can.*, *5b*(4), 398–409, doi:10.1139/f40-041.
Venegas, R. M., P. T. Strub, E. Beier, R. Letelier, A. C. Thomas, T. Cowles, C. James, L. Soto-Mardones, and C. Cabrera (2008), Satellite-derived variability in chlorophyll, wind stress, sea surface height, and temperature in the northern California Current System, *J. Geophys. Res.*, *113*, C03015, doi:10.1029/2007JC004481.
Visser, A. W. (1997), Using random walk models to simulate the vertical distribution of particles in a turbulent water column, *Mar. Ecol. Prog. Ser.*, *158*, 275–281.
Werner, F. E., and B. M. Hickey (1983), The role of a longshore pressure gradient in Pacific Northwest coastal dynamics, *J. Phys. Oceanogr.*, *13*(3), 395–410, doi:10.1175/1520-0485(1983)013<0395:TROALP>2.0.CO;2.
Wetz, M. S., B. Hales, Z. Chase, P. A. Wheeler, and M. M. Whitney (2006), Riverine input of macronutrients, iron, and organic matter to the coastal ocean off of Oregon, U.S.A., during the winter, *Limnol. Oceanogr.*, *51*, 2221–2231.
Whitney, M. M., and J. S. Allen (2009), Coastal wind-driven circulation in the vicinity of a bank. Part II: Modeling flow over the Heceta Bank complex on the Oregon coast, *J. Phys. Oceanogr.*, *39*(6), 1298–1316, doi:10.1175/2008JPO3967.1.
Willmott, C. J. (1982), Some comments on the evaluation of model performance, *Bull. Am. Meteorol. Soc.*, *63*(11), 1309–1313, doi:10.1175/1520-0477(1982)063<1309:SCOTEO>2.0.CO;2.

© 2014. American Geophysical Union. All Rights Reserved.